The Integration and Applications of Organic Thin Film Transistors and Ferroelectric Polymers

Yu-Jen Hsu

Submitted in partial fulfillment of the
requirements for the degree of
Doctor of Philosophy
in the Graduate school of Arts and Sciences

Columbia University

2012

Abstract

The Integration and Applications of Organic Thin Film Transistors and Ferroelectric Polymers

Yu-Jen Hsu

Organic thin film transistors and ferroelectric polymer (polyvinylidene difluoride) sheet material are integrated to form various sensors for stress/strain, acoustic wave, and Infrared (heat) sensing applications. Different from silicon-based transistors, organic thin film transistors can be fabricated and processed in room-temperature and integrated with a variety of substrates. On the other hand, polyvinylidene difluoride (PVDF) exhibits ferroelectric properties that are highly useful for sensor applications. The wide frequency bandwidth (0.001 Hz to 10 GHz), vast dynamic range (100n to 10M psi), and high elastic compliance (up to 3 percent) make PVDF a more suitable candidate over ceramic piezoelectric materials for thin and flexible sensor applications. However, the low Curie temperature may have impeded its integration with silicon technology. Organic thin film transistors, however, do not have the limitation of processing temperature, hence can serve as transimpedance amplifiers to convert the charge signal generated by PVDF into current signal that are more measurable and less affected by any downstream parasitics.

Piezoelectric sensors are useful for a range of applications, but passive arrays suffer from crosstalk and signal attenuation which have complicated the development of array-based PVDF sensors. We have used organic field effect transistors, which are compatible with the low Curie temperature of a flexi-

ble piezoelectric polymer,PVDF, to monolithically fabricate transimpedance amplifiers directly on the sensor surface and convert the piezoelectric charge signal into a current signal which can be detected even in the presence of parasitic capacitances. The device couples the voltage generated by the PVDF film under strain into the gate of the organic thin film transistors (OFET) using an arrangement that allows the full piezoelectric voltage to couple to the channel, while also increasing the charge retention time. A bipolar detector is created by using a UV-Ozone treatment to shift the threshold voltage and increase the current of the transistor under both compressive and tensile strain. An array of strain sensors which maps the strain field on a PVDF film surface is demonstrated in this work.

The strain sensor experience inspires a tone analyzer built using distributed resonator architecture on a tensioned piezoelectric PVDF sheet. This sheet is used as both the resonator and detection element. Two architectures are demonstrated; one uses distributed directly addressed elements as a proof of concept, and the other integrates organic thin film transistor-based transimpedance amplifiers monolithically with the PVDF sheet to convert the piezoelectric charge signal into a current signal for future applications such as sound field imaging. The PVDF sheet material is instrumented along its length and the amplitude response at 15 sites is recorded and analyzed as a function of the frequency of excitation. The determination of the dominant frequency component of an incoming sound is demonstrated using linear system decomposition of the time-averaged response of the sheet using no time domain detection. Our design allows for the determination of the spectral composition of a sound using the mechanical signal processing provided by the amplitude response and eliminates the need for time-domain electronic signal processing of the incoming signal.

The concepts of the PVDF strain sensor and the tone analyzer trigger the idea of an active matrix microphone through the integration of organic thin film transistors with a freestanding piezoelectric polymer sheet. Localized acoustic pressure detection is enabled by switch transistors and local transimpedance amplification built into the active matrix architecture. The frequency of detection ranges from DC to 15KHz; the bandwidth is extended using an architecture that provides for virtually zero gate/source and gate/drain capacitance at the sensing transistors and low overlap capacitance at the switch transistors. A series of measurements are taken to demonstrate localized acoustic wave detection, high pitch sound diffraction pattern mapping, and directional listening. This system permits the direct visualization of a two dimensional sound field in a format that was previously inaccessible.

In addition to the piezoelectric property, pyroelectricity is also exhibited by PVDF and is essential in the world of sensors. An integration of PVDF and OFET for the IR heat sensing is demonstrated to prove the concept of converting pyroelectric charge signal to a electric current signal. The basic pyroelectricity of PVDF sheet is first examined before making a organic transistor integrated IR sensor. Then, two types of architectures are designed and tested. The first one uses the structure similar to the PVDF strain sensor, and the second one uses a PVDF capacitor to gate the integrated OFETs. The conversion from pyroelectric signal to transistor current signal is observed and characterized. This design provides a flexible and gain-tunable version for IR heat sensors.

Contents

List of Figures iv

Acknowledgements xviii

1 Introduction **1**

1.1 Thin film sensors - Pressure sensors, acoustic sensors and infrared heat sensors 1

1.2 Organic thin film transistors 3

1.2.1 Pentacene 3

1.2.2 TIPS-Pentacene 6

1.3 Ferroelectric polymer - Polyvinylidene difluoride 9

1.3.1 Poling of PVDF polymer and PVDF film properties . . 10

2 Strain Sensor **16**

2.1 Introduction 16

2.2 Device design 18

2.3 Fabrication process 21

2.4 Characterization and measurement 24

2.4.1 Measurement setup 24

2.4.2 Single device characterization 26

2.4.3 Power consumption 27

2.4.4 Control transistor - OFET on PVDF substrate with 20sec UV-Ozone treatment . . . 28
2.4.5 Strain field mapping . . . 29
2.4.6 Characterization of sensitivity . . . 29
2.4.7 Charge retention time . . . 30
2.5 OLED integrated strain sensor . . . 31
2.6 Conclusion of the chapter . . . 32

3 Tone Analyzer 40
3.1 Introduction . . . 40
3.2 Device design & Fabrication . . . 43
3.2.1 Distributed capacitor array type of tone analyzer . . . 43
3.2.2 Integrated organic transistor tone analyzer . . . 44
3.2.3 Fabrication process . . . 45
3.3 Characterization and measurement . . . 46
3.3.1 Measurement setup . . . 46
3.3.2 Full range scan . . . 47
3.3.3 The response matrix . . . 48
3.3.4 Deriving excitation frequency . . . 49
3.4 Conclusion of the chapter . . . 50

4 Arrayed Microphone 56
4.1 Introduction . . . 56
4.2 Design . . . 59
4.3 Fabrication process . . . 61
4.4 Measurement and characterization . . . 61
4.5 Conclusion of the chapter . . . 63

5 Infrared Pyroelectric Sensor 76

5.1 Introduction 76

5.2 Pyroelectric response of the PVDF sheet 77

5.3 The integration of OFET and PVDF - Floating gate type . . . 79

5.3.1 Device design & Fabrication process 79

5.3.2 Characterization of the floating gate OFET integrated PVDF IR sensor 81

5.4 The integration of OFET and PVDF - Metal gate type 83

5.4.1 Device design & Fabrication process 83

5.4.2 Characterization of the metal gate OFET integrated PVDF IR sensor 85

5.4.3 Flipping the absorber and the reflector 90

5.5 Conclusion of the chapter 92

6 Conclusion and Future Work 100

List of Figures

1.1 Pentacene, a polycyclic aromatic hydrocarbon consisting of five benzene rings, is one of the most popular and well-studied organic semiconductors. 4

1.2 A physical vapor deposition (PVD) system dedicated to the evaporation of pentacene. This system is designed and built by Zhang Jia, Vincent Lee, and Yu-Jen Hsu. 5

1.3 A variant of pentacene, 6,13-Bis(triisopropylsilylethynyl)pentacene (TIPS-Pentacene), is designed to have two Si-(CH3)3 bonds at the position of sixth and thirteenth to prevent the oxidation at the two most reactive sites. 6

1.4 I-V characteristics of a thin film transistor using thermally evaporated TIPS-Pentacene. The W/L ratio of the organic transistor is 1000μm/ 25μm. 7

1.5 (a) TIPS-Pentacene before thermal evaporation. A clear crystallic form can be observed from this picture. (b)Decomposed TIPS-Pentacene. It can be seen from this picture that the material in the crucible becomes smooth and shiny after thermal deposition. The crystallic form is replaced by amorphous form after the exothermic degradation (261-266°C), thus the transistors evaporated after the degradation cannot work properly. 8

1.6 Drop-casted TIPS-Pentacene, 4 percent in Toluene. Dipole moment and surface tension are the main causes which push the material to the edge when drying. 9

1.7 (a)HP inkjet system and the robot. A venturi pump is installed to provide the back-pressure for the inkjet tip (model no.21). The robot system is controlled by a customized LabVIEW program. CCD camera is used to identify the features and locate the dispensing spot. (b)A closer look of the HP inkjet head and the transistors on a glass substrate. 12

1.8 Parameters used in HP inkjet to print TIPS-pentacene. An Excel macro program allows the setting of all the parameters. 13

1.9 Inkjetted TIPS-pentacene thin film transistor on a flexible substrate. It can be seen that the TIPS-pentacene is only dispensed at the chosen transistor, thus cross-talk between devices can be effectively minimized. 14

1.10 I-V characteristic of a thin film transistor using inkjetted TIPS-pentacene. The W/L ratio of the tested transistor is 290μm/ 20μm. 14

1.11 The stick diagrams of the α-phase PVDF and the β-phase PVDF. 15

2.1 (a) The equivalent circuit of an OFET on PVDF. The measured C_{SD} is 0.42pF, and C_{S-ref} (capacitance between source to back reference electrode) is 1.06pF (measured with Agilent 4284A LCR meter @ 1KHz). C_{GS} and C_{GD} are both zero since no metal gate is used in this architecture. (b) The microscope image on the right shows the geometry and the dimension of the device. The width over length ratio of the transistor is 200 (W=3000μm, L=15μm). Source and drain layer is blanketed with pentacene and another layer of Parylene-C. Aluminum is deposited on the The back of the PVDF film to form a reference electrode. 20

2.2 The process flow used to fabricate the PVDF strain sensor using monolithically integrated OFETs. The PVDF sheet serves both as the sensing element and the substrate, and the OFETs provide transimpedance amplification of the charge signal produced by the piezoelectric actuation into a current signal. . . . 22

2.3 The completed 4 X 10 strain sensor array on PVDF substrate laminated to a PVC card. A printed circuit board interfaces the finalized device to the measurement apparatus. A robotic actuator deformed the PVC card from it neutral plane; and the current of all forty OFETs integrated with the PVDF film can be measured to map the strain field of the PVC card. . . . 25

2.4 (a) The measured source-drain current for a single device at V_{DS}=35V. The device is actuated at T = 50s and T = 150s, and is released at T = 100s and T = 200s. The time step is 200msec. (b) The source-drain current at V_{DS}=35V under different direction of deformation. When the sensor is actuated with a concave shape (compressive strain), the current level was decreased. While under convex actuation (tensile strain) of deformation, the current level was increased. This bipolar sensitivity is enabled by the more positively shifted threshold voltage, which prevents the transistor from entering the cut-off region. 33

2.5 (a) $I_D - V_{DS}$ curve of control transistor with 20 second UV-Ozone treatment. A control transistor is a transistor with metal gate, and it is fabricated directly on the PVDF substrate. UV-Ozone is applied to shift its threshold voltage. (b) $I_D - V_{GS}$ curve of the control transistor with 20 second UV-Ozone treatment. (c) Square root scale and log scale of $I_D - V_{GS}$ curve of the control transistor. 34

2.6 (a) 1-D Strain field mapping of a bent strain sensor attached to a plastic card on the Y-axis (longitudinal), showing the trend of the local strain. (b) 2-D Strain field mapping of a deformed strain sensor at the lower bottom area. The 2-D contour map indicates that at the middle bottom part of the plastic card, strain is more concentrated. (c) 2-D Strain field mapping of a twisted strain sensor. The 2-D contour map shows an oblique strain concentration that complies with the shape of the twisting. 35

2.7 Resistance of the OMEGA precision strain gage and the measured current of the PVDF strain sensor versus time. Three cycles of press and release at a speed of 2 inch/min from 0.001 inch to 0.8 inch in 240 seconds are applied to the testing sample. The two sensors are located at the same location on the PVC substrate but on different faces. The commercial strain sensor has been tested and proved to have the same response to compressed and tensile stress, so it is attached to the opposite face of the PVDF strain sensor to provide the actual strain level for reference. Note that a initial displacement of 0.001 inch is used to ensure the three cycles of measurement have the same direction of deformation. 36

2.8 Current change of the PVDF strain sensor versus actual strain level derived from the resistance change of the commercial strain gage. Three cycles of press and release are applied to the testing sample, and each cycle deforms the sample from 0.001 inch to 0.8 inch and back to 0.001 inch at a speed of 2 inch/min. A hysteresis during the release section of actuation is observed mainly due to the piezoelectric material charge relaxation. 37

2.9 I_D as a function of time, demonstrating gate charge retention. The gate charge follows a first order decay, and a tangent is shown as a guide to estimate the characteristic retention time. Actuation began at $T = 50$s, and 442 seconds of retention time was estimated through linear fitting of I_D. 38

2.10 OLED integrated with strain sensor. 38

2.11 The equivalent circuit of OLED integrated strain sensor. . . . 39

2.12 The picture of OLED integrated strain sensor. 39

3.1 The distributed capacitor array type tone analyzer. Fifteen top electrodes (aluminum) are patterned on the material opposite a common reference electrode (gold) on the other side of the piezoelectric sheet. A speaker is mounted underneath the device to excite the device. The white plastic rack uses three guitar tuners in order to tension the device. A low-stretch fishing line is used to apply tension to the resonator. The outline of the PVDF sheet been highlighted with a black line. 43

3.2 (a) Integrated organic transistor tone analyzer. Fifteen transistors are patterned on the PVDF sheet, opposite a common reference electrode (aluminum) on the opposite side of the piezo sheet. A speaker is used to excite the device. The white plastic rack uses three guitar tuners and low tension fishing line to tension the device at three points. The outline of the PVDF sheet been highlighted with a black line. (b) The design of the integrated organic transistor tone analyzer. (c) A single sensor element. The channel length of the transistor is 20μm, and the channel width is 3700 μm. 51

3.3 (a) Architecture I: Fabrication process of the distributed capacitor array type tone analyzer. (b) Architecture II: Fabrication process of the integrated organic transistor tone analyzer. 52

3.4 A measurement site (device)/frequency/current plot. The X-axis is the piezoelectric sensor device index. These are counted from 1 to 15, 1 is at the wide part of the triangle and 15 is at the tip. The Y-axis is the excitation frequency in Hertz, and the Z-axis is the amplitude of the measured piezoelectric response. 53

3.5 The measured AC piezoelectric response at 827Hz using the distributed capacitor array architecture. The average curve will be used to form the response matrix. 53

3.6 (a) The measured AC transistor response current at 630Hz along the 15 sensor elements using the integrated organic transistor tone analyzer. (d) The measured AC transistor response current at 827Hz along the 15 sensor elements using the integrated organic transistor tone analyzer. Ten measurements were taken to insure repeatability, and the average value is used to construct the 15x15 response matrix. The error bars show the standard deviation for each set of repeated measurements in the set. 54

3.7 15 curves of 15 random-picked non-harmonic frequencies with higher response versus the measured AC capacitive current at 15 sensing sites using the architecture of distributed capacitor are plotted. The 15x15 response matrix (R) is then formed by these fifteen curves. The responses are arranged from lower frequency to higher frequency (from top to bottom)in this graph. 55

3.8 The derived excitation vector of 827Hz. we can see the eighth frequency component has the highest weight number, so we know this shape and amplitude fit the eighth frequency the most, which is 827Hz. 55

4.1 Schematic process flow. The pre-poled PVDF (52 microns thick) serves as both the main sensing material and substrate for this device. The switch transistor gate is deposited and patterned, followed by the gate/sensor dielectric, the source/drain and reference electrodes, and the active semiconductor. A layer of parylene-C on top of the final device serves as the passivation at the end. 64

4.2 The 8X8 active matrix PVDF sensor, X-axis selection is done by switching the gate of the switch transistor on and off with a -20V voltage supply, and Y-axis selection is done by switching the source drain bias (-20V). The switch transistor shares its drain electrode with the source electrode of the sensor transistor. 65

4.3 The cartoon of a single device. A switch transistor with metal gate is designed to share its drain with the source of the the sensor transistor on its right, which has a larger W/L ratio. . . 66

4.4 The equivalent circuit model of the PVDF microphone. The PVDF film in this model is simulated as a capacitor, and the capacitance is determined by the dimension of the metalized area and the thickness of parylene-c and PVDF. Due to the row and column interconnects, the switch transistor is loaded with a parasitic capacitance as shown in the top right dashed block and the sensor transistor is loaded with a parasitic capacitance as shown in the bottom right dashed block of this diagram. . . 67

4.5 The measurement arrangement for Fig. 4.6 and Fig. 4.7. The tube provides the localized air flow used to demonstrate the localization of the piezoelectric response. 68

4.6 A localized map of turbulent air flow from a tube directed to the microphone. This 2D surface map is made with an interpolation factor of 4. The active matrix allows measurement from each of the 64 sites individually. The compressed air current is introduced on four different location on the PVDF microphone sample. Our measurement shows that the PVDF microphone can map the distribution of the compressed air pressure. Edge-induced turbulence from the circuit board can be seen in (5,5), which is the bottom right figure. The microphone can accurately detect the location of the highest level of excitation, which is the spot where the compressed air is applied, as well as the downstream air flow and boundary-related turbulence. 69

4.7 The time domain response of a single switched transistor element in response to a stream of compressed gas. The onset of the compressed gas is at 0.9 seconds on the time axis. A large turn-on transient is observed due to the surface deflection, and the interaction of the boundary layer with the piezoelectric generates a charge response which is communicated as a current through the switch and interconnect network. This excitation represents a broadband noise source. The RMS response after the transient is plotted in Fig. 4.6. 70

4.8 The noise floor of the measurement derived from the pre-excitation part of Fig. 4.7. The square root of power versus frequency is plotted here. The noise comes from room acoustic noise, measurement instruments noise, and noise from the switch transistors. 71

4.9 Signal frequency composition of the response derived from the post-excitation part of Fig. 4.7. Signal to noise ratio is estimated to be 100 to 1 by comparing this graph with Fig. 4.8, and it reaches 1 when the frequency is around 15kHz, which shows the bandwidth of this device. 71

4.10 An acoustic diffraction pattern at 12kHz (2.9cm) of the amplitude response is plotted here for all 64 sites in interpolated (factor of 4) false color. The dashed lines indicate the interference pattern, which are consistent with the expected fringe spacing. 72

4.11 The measurement setup for the acoustic diffraction experiment. Two commercially available audio speakers are synchronized in phase and are placed at opposing corners of the microphone to generate the diffraction pattern. 73

4.12 The sensitivity curve of the active matrix PVDF microphone element device. Sound pressure is calibrated by using G.R.A.S 40PH microphone. Our device is characterized to have a sensitivity of sound pressure to 9.5nA/Pa. 74

4.13 Unnormalized frequency response of the active matrix PVDF microphone element device. An off-the-shelf speaker is used here. Our device showed a frequency response covering the whole acoustic range. The peaks showing in the frequency response plot is coupling with the frequency response of the speaker. 75

5.1 Pyroelectric response of a PVDF film coated with 180 $\AA$ of sputtered Au/Pd electrodes measured with a lock-in amplifier (Standford Research, SR-830). The integration time of the lock-in amplifier is 300 mS, and the sensitivity is set at 50 mV. An incandescent light bulb is used as the IR source and is chopped at 4HZ. 78

5.2 Pyroelectric IR sensor. (a) The process flow of an integrated OFET and PVDF sensor element. (b) The schematic diagram of IR excitation to the pyroelectric IR sensor. 80

5.3 PVDF pyroelectric sensor. 81

5.4 (a)The HawkEye IR-18 IR source.(b) The IR profile visualized using temperature sensitive thermochromic sheet (color changing range: 35°C-40°C). 82

5.5 Pyroelectric response of the floating gate OFET integrated PVDF IR sensor. 83

5.6 The comparison between the current under no stimulation (blue), single shutter open (red), and multiple shutter opens and closes (yellow). Hawkeye IR-18 IR source is used and biased at 8V. 84

5.7 The metal gate OFET integrated PVDF IR sensor. The sensing region is isolated and the parylene layer is patterned. . . . 85

5.8 The measurement setup of the pyroelectric IR sensor. The aluminum foil shutter is controlled by a stepper motor, and the IR source is regulated to maintain a surface temperature lower than 55°C. 86

5.9 Time versus current characteristics at different shutter control conditions. The black curve shows the current response to room temperature, the red curve shows the response of shutter opened once, and the blue curve is the response of shutter opened and closed for two times. 89

5.10 The equivalent circuit diagram of the metal gate OFET integrated PVDF IR sensor. The discharging path is denoted with the red line in the diagram. 90

5.11 Time versus current characteristics at different temperature stimulations 93

5.12 Current change versus temperature change. It can be estimated that the responsivity is 3.8nA/°C. 94

5.13 The IR sensor with Al gate and Au/Pd absorber. The pentacene is fully covered by the aluminum layer, so the IR excitation will be reflected. 95

5.14 The I$_{ds}$-V$_{ds}$ characteristics of the UV-Ozone treated transistor. 96

5.15 The I_{ds}-V_{gs} characteristics of the UV-Ozone treated transistor. V_{ds} is biased to -20V. 96

5.16 The current response of the IR sensor stimulated with a IR source biased at 4V(surface temperature = 29°C). 97

5.17 The current response to different temperatures, dependence of the IR sensor. The current is normalized to see the change in terms of slope. A shutter made of a sheet of aluminum foil opened at 2.8 second. Room temperature measured by a thermocoupler attached to the PVDF sheet is 24°C. 98
5.18 The slope (0.15 second after the shutter is opened) of the current response versus surface temperature. A trend of decreased slope is observed as the source temperature increases. 99

Acknowledgements

This work was supported by the National Science Foundation under Award ECCS-0644656 and by the Defense Advanced Research Project Agency through program manager Dr. Akintunde I. Akinwande of the Microsystems Technology Office.

The author thank M. Thompson of Measurement Specialties Inc. for the PVDF sheet used in this study.

The author also thank all the members in the Columbia Laboratory of Unconventional Electronics, especially to Prof. Ioannis Kymissis, Dr. Nadia Pervez, Dr. Brain Tull, Dr. Sung-Jim Kim, Dr. Zhang Jia, Vincent Lee, John Sarik, Samuel Subbarao, Haig Norian, Marshall Cox, Jonathan Beck, Hassan Edress, Hisn-Jung Lee, Shyuan Yang, Yasmin Afsar, Zeynep Barsaran, and Fabio Carta for the guidance, assistance and patience.

Special thanks to Vincent Lee for the proof-reading and editing.

To my parents, and to everyone who has given me a hand when I was in need.

Chapter 1

Introduction

1.1 Thin film sensors - Pressure sensors, acoustic sensors and infrared heat sensors

Thin film sensors have drawn a considerable attentions in recent years with the growing demands from many research areas including robots, portable devices, energy-harvesting appliances, health care instruments, mass-transportation vehicles, and weapons systems. Among all kinds of different sensors, three categories will be discussed in the research: pressure sensors, sound sensors, and infrared temperature sensors.

Pressure sensors are particularly useful for human interface devices and the electronic skin of robot application. A single pressure sensor unit can detect stress and strain and convert the mechanical actuation into an electrical signal, and a 2-D array of pressure sensors not only reads the value of stress and strain of each local site, but also maps the distribution of the stress and strain over an area. A 2-D array of pressure sensors are suitable for applications which require one to pinpoint where the maximum loading spot is and to visualize the stress/strain profile of an area. For smaller sized sensors can be used for medical applications, whereas, larger format sensors can be practical for structural health monitoring or traffic control applications.

Since variations in air pressure is the origin of sound, a pressure sensor with high responsivity and proper frequency response can be applied to acoustic sound sensing. This kind of sensors can contribute to the development of all kinds of acoustic sensor devices and even biomimetic devices. By reading the intensity and visualizing the profile of sound wave in time domain, one can determine sound frequency and analyze the sound source. A sound sensor array is especially advantageous to noise field analysis, non-destructive testing, and source localization.

Another kind of sensor which shares equal importance is the infrared(IR) heat sensor. A highly sensitive IR sensor is especially useful for human body temperature sensing, and this sensing technique can be applied to, for example, passenger body temperature monitoring in the airport or personal belongings screening for security check. Besides, motion sensing can also one of the major applications for IR sensors. A stimulation of heat triggers the IR sensor which then signals the integrated system with electrical pulse. This device can be used for household security and for military purposes.

Here we are proposing an integration of ferroelectric polymer, polyvinylidene difluoride (PVDF), and organic thin film transistors (Pentacene-based) to perform stress/strain sensing, acoustic sound sensing, and infrared heat sensing. Organic transistors, with the room temperature fabrication process and the ease of integration to various substrate, are considered to be one of the most suitable candidates to carry out tasks that are previously inaccessible to silicon-based transistors.

1.2 Organic thin film transistors

1.2.1 Pentacene

Among all of the organic semiconductors, pentacene is one of the most popular and well-studied small molecule materials for organic thin film transistors. In fact, the members of the series of acenes exhibit semiconductor characteristics because of their conjugated structure. The energy gap of pentacene (five benzene rings) is 2.1eV, and it is lower than that of teracene (four benzene rings, 2.6eV), anthracene (three benzene rings, 3.3eV), and Napthalene (two benzene rings, 4.3eV). [**?**]

This phenomena of lower energy gap as the number of benzene rings increases is a result of the mechanism of carrier transportation in organic semiconductors. The energy gap defined here is the difference between the highest occupied molecular orbital (HOMO) and the lowest unoccupied molecular orbital (LUMO).

Although the exact carrier transport mechanism is still under debate, we believe the carrier transport mechanism is closely related to the charge hopping between localized states of individual molecules.

Pentacene, a polycyclic aromatic hydrocarbon consisting of five benzene rings as shown in Fig. 1.1, is categorized as a P-type organic semiconductor and holes are the majority charge carriers. The characteristics of pentacene have been studied by many groups. The energy gap of pentacene is estimated and measured to be 2.1eV, and an maximum mobility is reported to be over

5 cm^2/V.s, [?] [?] [?] which is comparable to the mobility of amorphous silicon. High carrier mobility makes pentacene the most favorable material for organic thin film transistors. The synthesis and purification process has also been throughly researched. [?] Pentacene is selected as the main organic semicondutor for thin film transistors in this research.

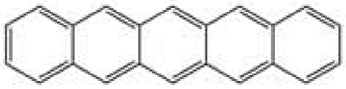

Figure 1.1: Pentacene, a polycyclic aromatic hydrocarbon consisting of five benzene rings, is one of the most popular and well-studied organic semiconductors.

The effectiveness of pentacene-based transistors is strongly determined by the morphology of the pentacene film. One of the common problems using pentacene as the active material for a thin film transistor is controlling the grain sizes. When the grain size of pentacene is too small, the current flowing from the source electrode to the drain electrode will be affected by the grain boundaries and the value will be decreased. Usually smaller grain occurred at the interface between the source/drain electrodes and the dielectric due to the discontinuity of material and the difference of surface energy. Surface treatment using self-assembly monolayers (SAMs) can help improving the grain boundary issue by forming monolayers covering the whole contact region of pentacene. In this research, Pentafluorobenzenethiol is used for surface treatment. Thiols attaches to gold (source/drain electrode), and that builds a low surface energy layer on the source and drain formed by gold. Consequently, gold electrodes and the dielectric layer will have similar surface energy after

SAMs treatment, and the morphology of pentacene will be much favorable to carrier transportation. The performance of device after surface treatment is observed to be much improved. [?]

Thermal evaporation in a high-vacuum environment is the most reliable and well-developed method to deposit pentacene. A physical vapor deposition (PVD) system (as shown in Fig. 1.2) is built for this purpose, and its vacuum level reaches 1×10^{-8} torr with the help of a turbo pump backed by a scroll pump. A deposition rate of 1 angstrom/sec is controlled by a source temperature controller during the deposition process to ensure a high quality pentacene deposition in terms of morphology and mobility. [?]

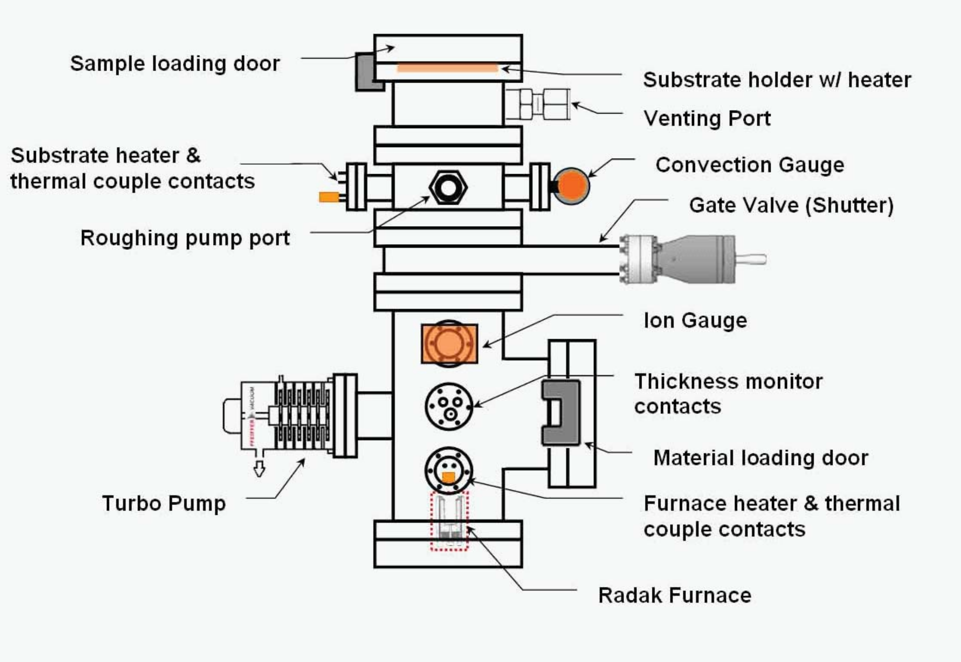

Figure 1.2: A physical vapor deposition (PVD) system dedicated to the evaporation of pentacene. This system is designed and built by Zhang Jia, Vincent Lee, and Yu-Jen Hsu.

1.2.2 TIPS-Pentacene

The sixth and thirteenth position of pentacene is particularly reactive to water and oxygen. However, a variant of pentacene, 6,13-Bis(triisopropylsilylethynyl)pentacene (TIPS-Pentacene), is engineered to have two Si-(CH3)3 bonds at the sixth and thirteenth position to form passivation and protect the most reactive sites. [?] The molecular structure of TIPS-Pentacene is shown in Fig. 1.3. [?]

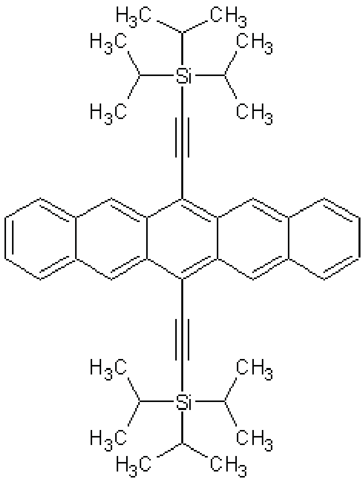

Figure 1.3: A variant of pentacene, 6,13-Bis(triisopropylsilylethynyl)pentacene (TIPS-Pentacene), is designed to have two Si-(CH3)3 bonds at the position of sixth and thirteenth to prevent the oxidation at the two most reactive sites.

TIPS-Pentacene can be deposited either through a thermal evaporation process or a solution process. Current-Voltage characteristics of a thin film TIPS-Pentacene transistor using thermal deposition is shown in Fig. 1.4. The W/L ratio of the transistor is 1000μm/ 25μm. The PVD used for pentacene deposition is also used here for TIPS-Pentacene deposition. Overall, the performance of these transistors is better than that of the transistors with

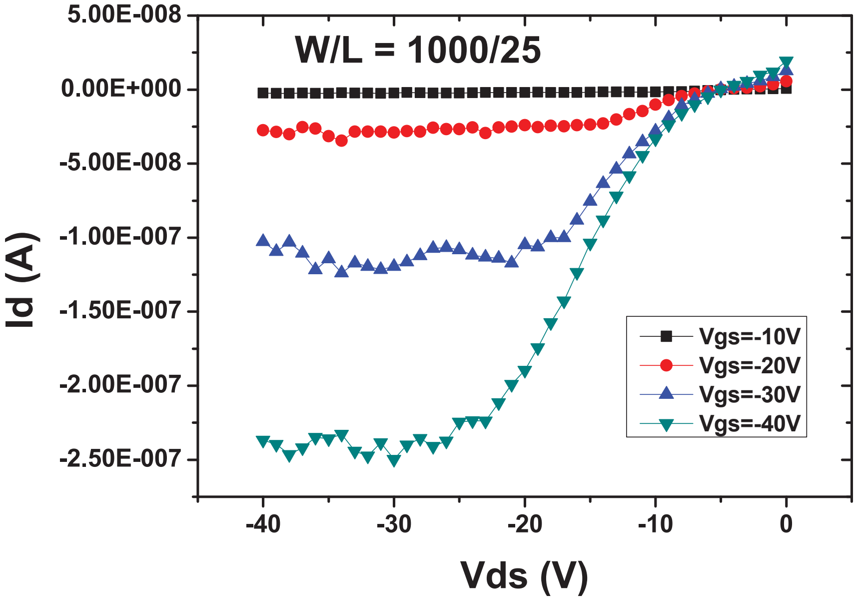

Figure 1.4: I-V characteristics of a thin film transistor using thermally evaporated TIPS-Pentacene. The W/L ratio of the organic transistor is 1000μm/ 25μm.

regular pentacene. However, exothermic degradation limits the life time of TIPS-Pentacene in the crucible of a thermal evaporator. The crystalline form of TIPS-Pentacene transforms to an amorphous phase after a thermal evaporation above 260°C. The decomposed TIPS-Pentacene in an evaporation crucible is shown in Fig. 1.5. [?] Therefore, refilling material is required each time before deposition. This extends the total processing time and compromises the vacuum of the chamber.

TIPS-Pentacene has good solubility in common organic solvents (tetralin, toluene, etc.). Methods of drop-cast and inkjet printing can both be performed to deposit TIPS-Pentacene. [?] Drop-casted TIPS-Pentacene in Toluene is shown in Fig. 1.6. This method has also been proven to be successful for

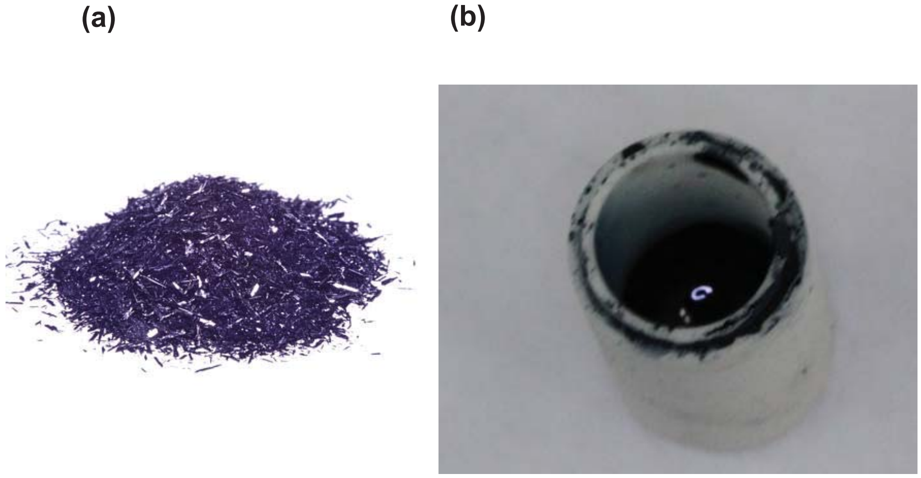

Figure 1.5: (a) TIPS-Pentacene before thermal evaporation. A clear crystallic form can be observed from this picture. (b)Decomposed TIPS-Pentacene. It can be seen from this picture that the material in the crucible becomes smooth and shiny after thermal deposition. The crystallic form is replaced by amorphous form after the exothermic degradation (261-266°C), thus the transistors evaporated after the degradation cannot work properly.

fabricating transistors.[?] However, patterning TIPS-Pentacene is a challenge when drop-cast method is used.

Inkjet printing is also considered one of the most promising techniques for the fabrication of organic transistors. Beacuase inkjet printing is an additive process, patterning TIPS-pentacene is as simple as selecting where to print. In this research, a HP thermal inkjet system is installed on a three axis stage to perform inkjet printing of TIPS-Pentacene. The setup is shown in Fig. 1.7. A thin-film transistor using inkjetted TIPS-pentacene is shown in Fig. 1.9, and its I-V characteristic is plotted in Fig. 1.10. The parameters used

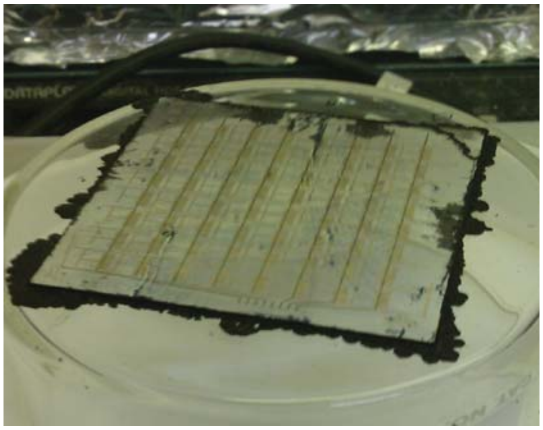

Figure 1.6: Drop-casted TIPS-Pentacene, 4 percent in Toluene. Dipole moment and surface tension are the main causes which push the material to the edge when drying.

for TIPS-pentacene inkjet priniting is recorded and is shown in Fig. 1.8.

In general, inkjet printing is preferred for TIPS-pentacene deposition in this work. A 2% (by weight) TIPS-pentacene in tetralin sloution is used for the deposition. The performance of the transistors is not limited by the exothermic degradation seen in thermal evaporation, and TIPS-pentacene can be patterned to minimize the cross-talk between devices.

1.3 Ferroelectric polymer - Polyvinylidene difluoride

Polyvinylidene difluoride (PVDF, (-($C_2H_2F_2$)-)), the ferroelectric polymer which is the sensing material and the substrate for this research, was first discovered by Kawai[**?**] in 1969. PVDF is a linear polymer with a carbon backbone and two dipole moments (CH_2 and CF_2) in each monomer unit. Several crystal phases are exhibited by PVDF including alpha(TGTG'), beta(TTTT), and gamma(TTTGTTTG') crystalline phases ('T' stands for trans linkages and 'G' stands for gauche linkages). [?]

Beta-phase is the most common and most studied form for its piezoelectricity and pyroelectricity. This all-trans conformation of beta-phase has the most aligned dipoles and thereby yields the maximum possible saturation polarization. [?] [?] The piezoelectric constant, d_{33}, of PVDF, different from most piezoelectric materials, is a negative number. So the reactions of common piezoelectric materials are usually opposite to that of PVDF. The crystalline phase of PVDF has been studied by several authors, and it is agreed by several authors that the beta-phase PVDF film peaks at $2\theta = 20.7°$ when characterized with a X-ray diffractometer. [?] The conformation of the beta-phase has the most aligned dipoles and thereby yields the maximum possible saturation polarization. [?] [?]

1.3.1 Poling of PVDF polymer and PVDF film properties

When PVDF is poled by either mechanical rolling or stretching, the alpha-phase in the films transform to beta-phase. Beta-phase of PVDF exhibits piezoelectric and pyroelectric properties that are useful for sensor applications. In the form of conformation, hydrogen atoms are all on one side of the backbone while the fluorine atoms are on the other side. The early work on beta-phase PVDF also showed that it is possible to polarize PVDF to beta-phase by applying electric field while the temperature is held at $\sim$375K. Both methods can effectively polarize the PVDF polymer film to a desired phase. Our 52 micron-thick PVDF polymer is provided by Measurement Specialties

Inc., and is factory poled through the application of surface tension. The film is tested to confirm its beta-phase behavior, and Table 1.1 contains the essential parameters of the PVDF film we are using in this research.

Table 1.1: Properties of PVDF film

Symbol	**Parameter**	**Value**	**Units**
t	Thickness	52	μm
d_{31}	Piezo constant	23×10^{-12}	C/N
d_{33}	Piezo constant	-33×10^{-12}	C/N
g_{31}	Piezo stress constant	216×10^{-3}	$\frac{V}{N/m}$
g_{33}	Piezo stress constant	-330×10^{-3}	$\frac{V}{N/m}$
C	Capacitance	380	$\frac{pF}{cm^2}$ @1KHz
Y	Young's Modulus	3×10^9	$\frac{N}{m^2}$
p	Pyroelectric Coefficient	30×10^{-6}	$\frac{C}{m^2}$ °K
ϵ	Relative permitivity	12	–
ρ	Volume Resistivity	$> 10^{13}$	Ohm meters
ρ_m	Mass Density	1.78×10^3	$\frac{kg}{m}$
–	Maximum operating voltage	~ 30	MV/m, DC @25°C
–	Breakdown voltage	~ 80	MV/m, DC @25°C
–	Acoustic impedance	2.7×10^6	$\frac{kg}{m^2-sec}$
–	Temperature range	-40 to 100	°C

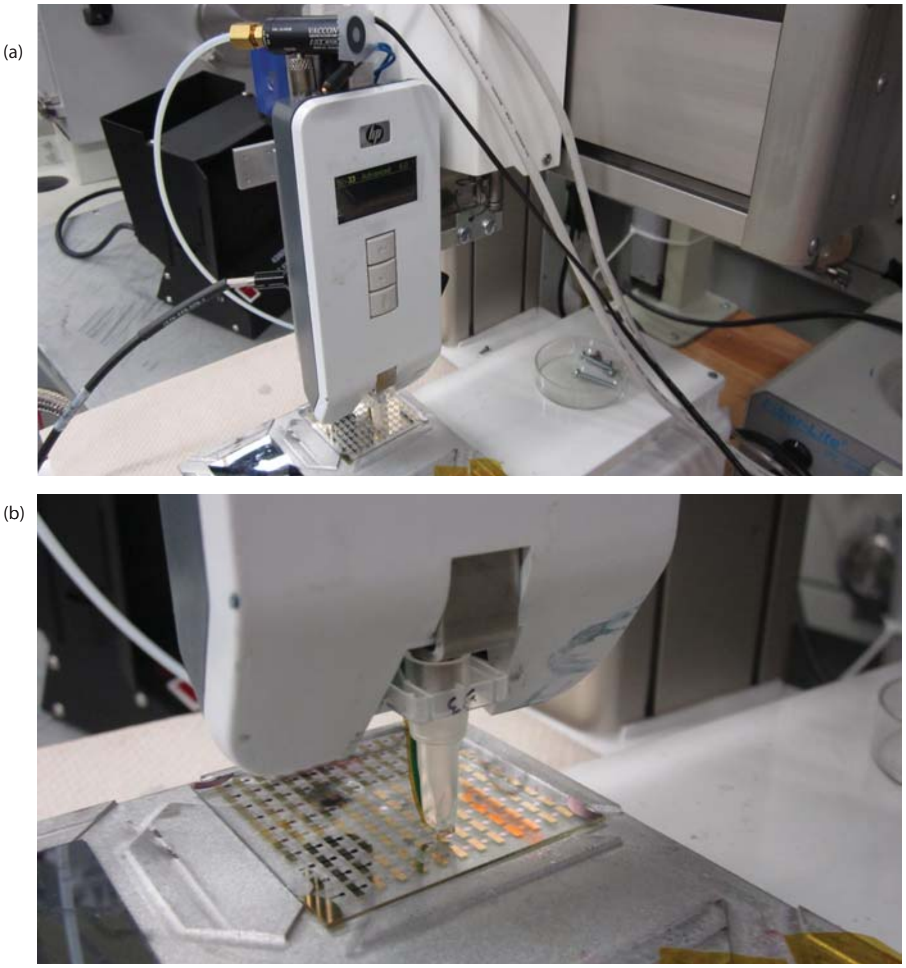

Figure 1.7: (a)HP inkjet system and the robot. A venturi pump is installed to provide the back-pressure for the inkjet tip (model no.21). The robot system is controlled by a customized LabVIEW program. CCD camera is used to identify the features and locate the dispensing spot. (b)A closer look of the HP inkjet head and the transistors on a glass substrate.

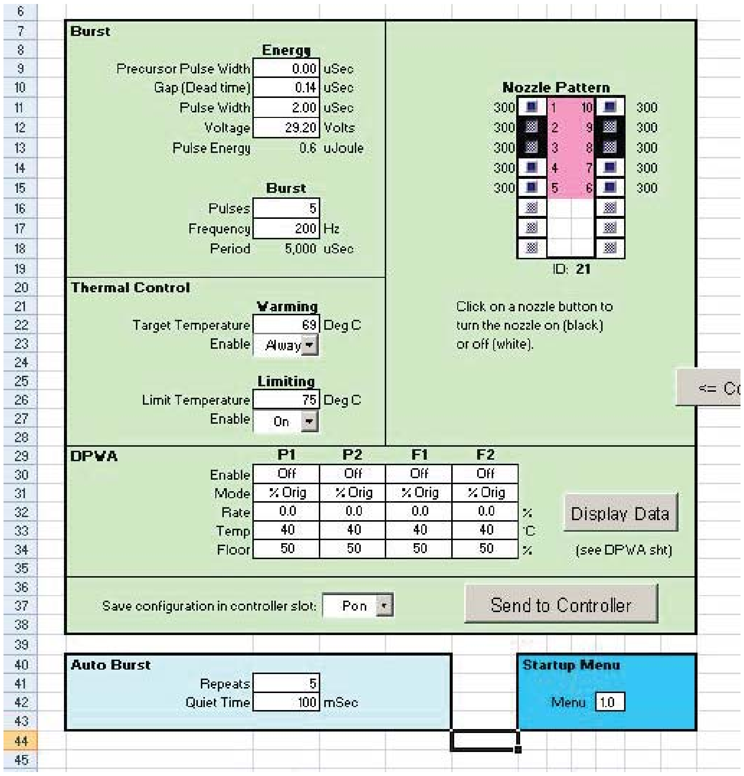

Burst

Energy		
Precursor Pulse Width	0.00	uSec
Gap (Dead time)	0.14	uSec
Pulse Width	2.00	uSec
Voltage	29.20	Volts
Pulse Energy	0.6	uJoule

Burst		
Pulses	5	
Frequency	200	Hz
Period	5,000	uSec

Thermal Control

Warming		
Target Temperature	69	Deg C
Enable	Away	

Limiting		
Limit Temperature	75	Deg C
Enable	On	

Nozzle Pattern

ID: **21**

Click on a nozzle button to turn the nozzle on (black) or off (white).

DPWA

	P1	P2	F1	F2	
Enable	Off	Off	Off	Off	
Mode	% Orig	% Orig	% Orig	% Orig	
Rate	0.0	0.0	0.0	0.0	%
Temp	40	40	40	40	°C
Floor	50	50	50	50	%

(see DPWA sht)

Save configuration in controller slot: Pon

Auto Burst

Repeats	5	
Quiet Time	100	mSec

Startup Menu

Menu 1.0

Figure 1.8: Parameters used in HP inkjet to print TIPS-pentacene. An Excel macro program allows the setting of all the parameters.

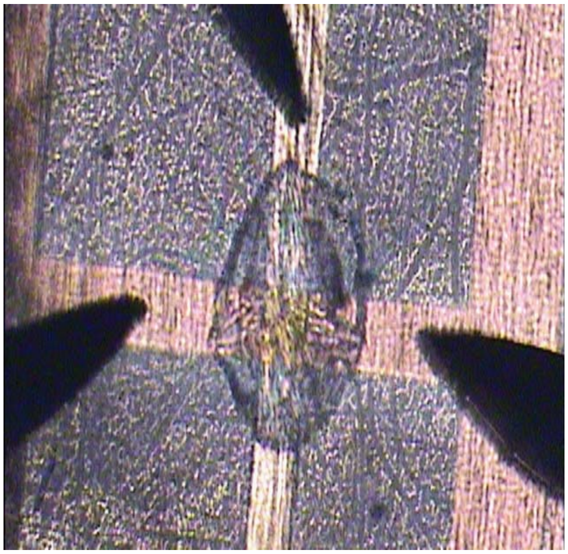

Figure 1.9: Inkjetted TIPS-pentacene thin film transistor on a flexible substrate. It can be seen that the TIPS-pentacene is only dispensed at the chosen transistor, thus cross-talk between devices can be effectively minimized.

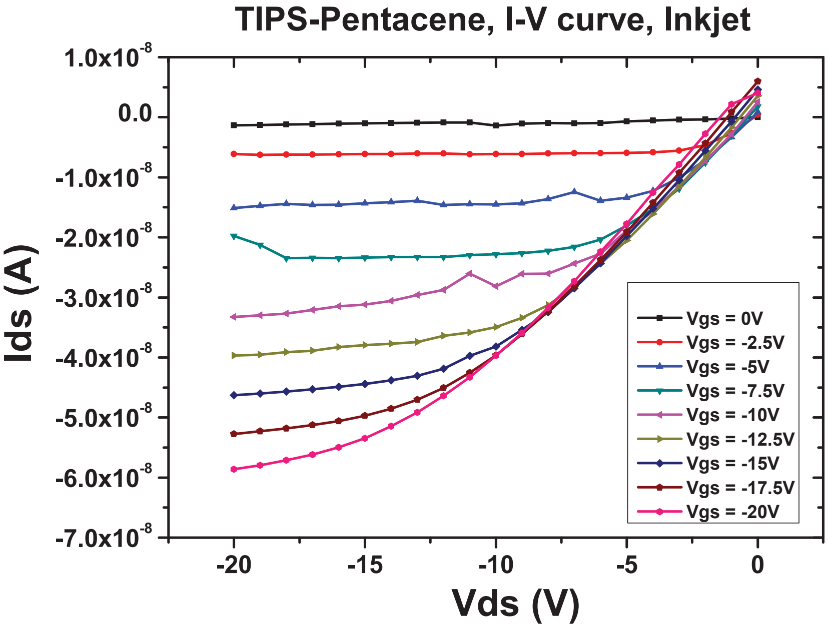

Figure 1.10: I-V characteristic of a thin film transistor using inkjetted TIPS-pentacene. The W/L ratio of the tested transistor is 290μm/ 20μm.

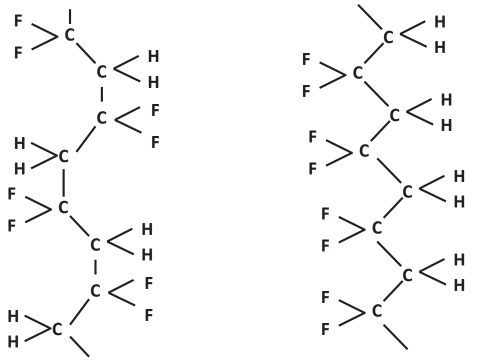

TGT$\bar{\text{G}}$ Conformation
α-phase PVDF

TT Conformation
β-phase PVDF

Figure 1.11: The stick diagrams of the α-phase PVDF and the β-phase PVDF.

Chapter 2

Strain Sensor

2.1 Introduction

Piezoelectric sensors have found a large number of applications including health care [?] and structural health monitoring [?]. The discovery of piezoelectric properties in the polymer polyvinylidene difluoride (PVDF) by Kawai, et al. [?] accelerated development in piezoelectric devices; piezoelectric polymers have a number of advantages over ceramic piezoelectric materials in some applications including high achievable peak strain, conformability to flexible surfaces, and a better acoustic impedance match to water [?] than ceramic piezoelectric systems.

Several array sensors have been developed to map strain and pressure on surfaces. Reston, et al. [?] and Kolesar, et al. [?] have demonstrated a pressure sensitive array sensor fabricated by laminating a layer of PVDF onto an array of crystalline silicon field effect transistors also integrated with amplification circuitry. Several approaches to making a flexible sensor skin have also been demonstrated. An active matrix mechanically flexible pressure sensor using a conductor loaded elastomer whose resistance changes with applied pressure has been demonstrated by Someya et al. [?]. This sensor device was especially notable because of its use of mechanically flexible organic field effect transistors to create the active matrix and addressing circuitry. A range of other flexible devices based on strain gauges [?], resistive sensor elements [?], and thermal strain sensors [?] have also been demonstrated.

One challenge to fabricating large area piezoelectric sensing devices using piezoelectric sheet materials over large areas is the parasitic capacitance which results from coupling to counter-electrodes, other devices, the structure being measured, or, if an active matrix array is being used, to other transistors and interconnects in the active matrix structure. This parasitic coupling both dissipates the voltage signal which the charge generated by the piezoelectric element produces, and also prevents localization of the surface strain on the structure. A solution to both of these problems is to use a transimpedance amplifier: converting the piezoelectric signal from a charge signal into a current signal. Given enough time to charge the parasitic capacitances, a current signal can overcome large capacitance and be extracted from the array. By localizing the area over which the charge is collected, spatial localization can also be achieved independent of other capacitive coupling into the interconnect lines.

Organic field effect transistors (OFETs) are ideal candidates to perform this transimpedance amplification on flexible polymer sheet piezoelectrics. OFETs are mechanically flexible, allowing for direct integration with flexible polymer materials. PVDF and related materials have a relatively low Curie point, 80°C [?]; temperature cycling above this temperature changes the crystal phase of the material and destroys its piezoelectric properties. OFETs can be lithographically fabricated at significantly lower temperatures, allowing fabrication on the piezoelectric material itself and formation of a monolithically integrated sensing structure. This allows a mechanically flexible amplified strain sensor to be built with direct coupling to the transistor. Other thin film transistor technologies require higher temperature tolerant substrates and need to be laminated to PVDF which impacts the mechanical flexibility and limits potential applications.

Ji et al. have demonstrated a hybrid laminated PVDF/OFET structure on a sheet polymer foil which reduces the parasitic capacitance traditionally seen coupling to silicon substrates by fabricating the structure on an insulating plastic [**?**]. Stadlober et al. demonstrate sensing both through use of a piezo/pyroelectric gate dielectric and a hybrid attached sensing element to an OFET [**?**] [**?**]. The architecture presented here monolithically integrates the structure directly on the PVDF sheet, further reduces the effect of the parasitic capacitance by eliminating the conductive gate, and allows measurement under both tension and compression by using a transistor whose V_T has been shifted in the positive direction. We also demonstrate strain mapping on a flexible object in the presence of significant capacitive loading of the interconnects, taking advantage of the long charge retention time of the conducting gate-free architecture.

2.2 Device design

Inspired by the integration of piezoelectric polymers and OFETs in prior work, we have developed an architecture that improves performance and processability. The first major change is the introduction of a metal gate-free structure during the fabrication process to reduce the effective overlap capacitance, C_{GD} and C_{GS}. This parasitic is problematic for piezoelectric sensing devices, especially as devices scale in size and an increasing design rule needs to be incorporated to accommodate substrate size changes during processing. This parasitic, which is through the high-capacitance gate dielectric, decreases the bandwidth of the sensor and allows parasitic charge sharing between the the channel (which is productive and leads to a sensing function) and the parasitic C_{GD} and C_{GS} capacitors (which reduce the effective bias on the device). Our design eliminates the metal gate layer and directly couples the transistor to the PVDF substrate. C_{GD} and C_{GS} are effectively zero. The equivalent circuit and microscope image are shown in Fig. 2.1. This approach also maximizes the charge retention time; a single point of failure in the gate dielectric is not fatal to charge retention in the device since there is no lateral conductivity in the gate.

The transconductance of OFETs on PVDF substrates is not as good as the performance of control OFET devices on a glass substrate due to the surface roughness of the pre-poled PVDF film. The morphology of pentacene on a PVDF substrate is not comparable to that of pentacene on a clean glass substrate. A UV-Ozone treatment [**?**], which shifts the threshold voltage in the positive direction, both increases the I_D and allows measurement of both compressive and tensile strain (i.e. both a positive and negative net charge) using a unipolar device.

The PVDF film for this application was cut into a 5cm by 5cm square. The source and drain of the OFET are formed by two identical 3mm by 0.5mm rectangles with a 15 μm channel in between; and a four by ten OFET array is integrated on the PVDF film. The finalized device is shown in Fig.

2.3 as the film that is laminated using a transfer adhesive to a white PVC card. The white PVC card provides a platform to perform identical and repeat tests.

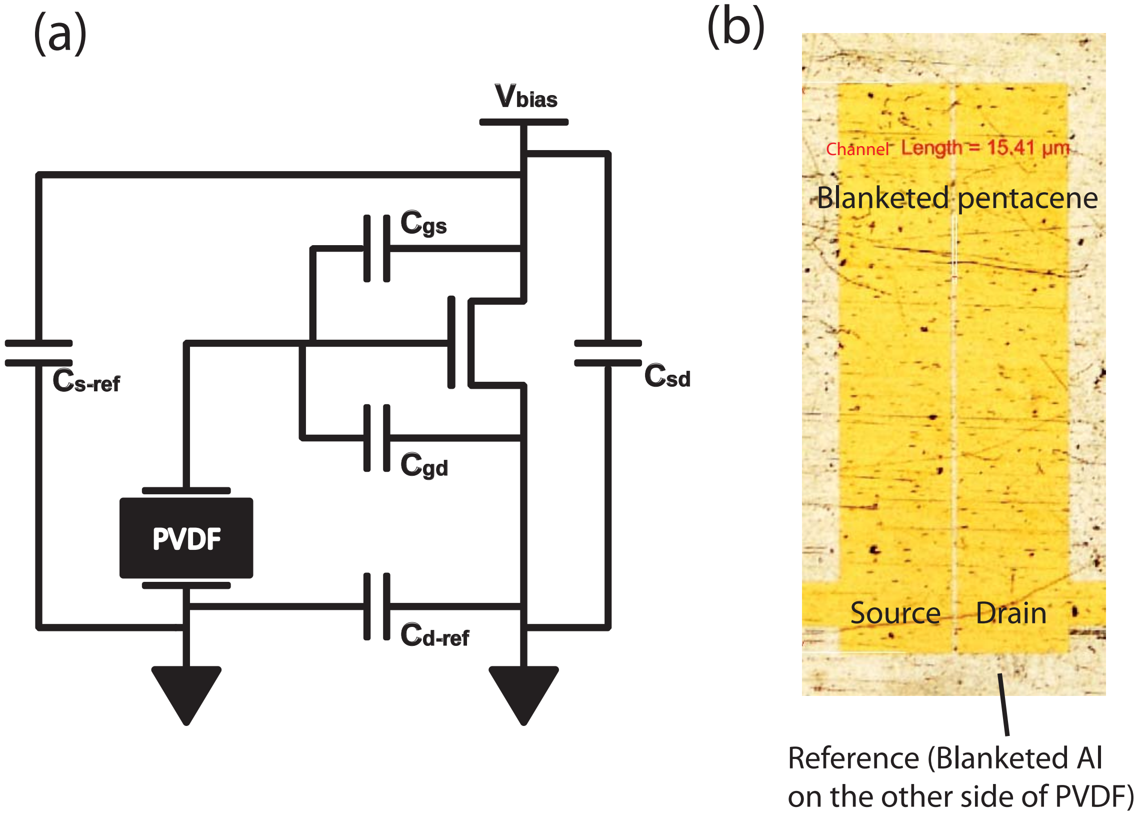

Figure 2.1: (a) The equivalent circuit of an OFET on PVDF. The measured C_{SD} is 0.42pF, and C_{S-ref} (capacitance between source to back reference electrode) is 1.06pF (measured with Agilent 4284A LCR meter @ 1KHz). C_{GS} and C_{GD} are both zero since no metal gate is used in this architecture. (b) The microscope image on the right shows the geometry and the dimension of the device. The width over length ratio of the transistor is 200 (W=3000μm, L=15μm). Source and drain layer is blanketed with pentacene and another layer of Parylene-C. Aluminum is deposited on the The back of the PVDF film to form a reference electrode.

2.3 Fabrication process

Performing photolithography on a sheet of flexible substrate is made possible by the surface tension of water drops. In the early stage, UV curable adhesives were used to glue the sample to a glass substrate in order to perform photoresist spinning and mask alignment, but this configuration limited the access to the back of the sample. Peeling the processed sample off the glass substrate was also a challenge, many of the fabricated samples were damaged during the peeling process, and the residues of the adhesives were hard to be removed completely. The air and water trapped in the interface of the sample and the glass substrate compromised the evaporator chamber vacuum and the performance of contact mask aligners. Therefore, four drops of deionized water dispensed at the four corners of a 5cm by 5cm glass substrate were used to hold the flexible PVDF sheet in place. The back of the sample became accessible for the deposition of materials, photoresist spinning and mask alignment were successful, and peeling the processed sample off the glass substrate was also fairly simple. This technique became the standard process for the photolithography on PVDF substrate.

The organic thin film transistor arrays are directly fabricated photolithographically on PVDF sheet as shown in Fig. 2.2. The process is based on the flow demonstrated by Kymissis et al. [?]

Oriented and poled PVDF film was provided by Measurement Specialties, Inc. The back of the PVDF sheet was metalized using 35nm of unpatterned aluminum to provide a reference (ground) electrode for the measurement. Some important properties of the PVDF extracted from table 1.1 is listed in table 2.1. Solvent cleaning was performed before the fabrication process.

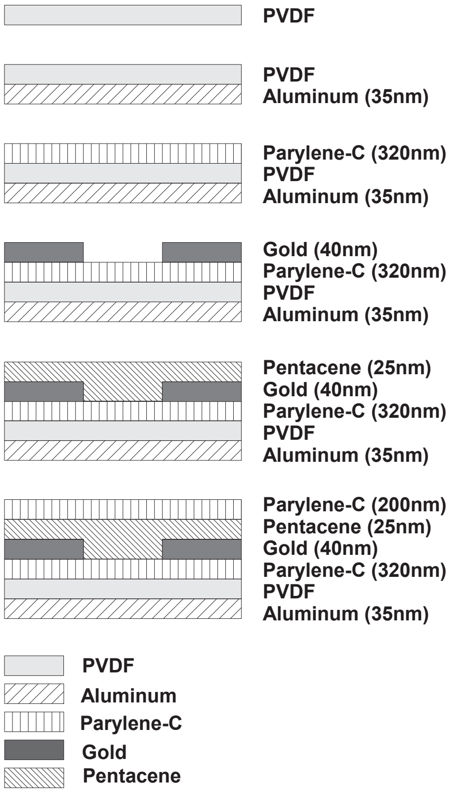

Figure 2.2: The process flow used to fabricate the PVDF strain sensor using monolithically integrated OFETs. The PVDF sheet serves both as the sensing element and the substrate, and the OFETs provide transimpedance amplification of the charge signal produced by the piezoelectric actuation into a current signal.

Avoid creating dead spots on the PVDF sheet is important, and this can be done by controlling the pressure of the air blow onto the substrate when drying the sample.

320nm(measured with a profilometer) of parylene-C (∼0.25g) was CVD deposited on the PVDF surface. The furnace temperature of the CVD was held at 690° while the vaporizer evaporated the dimers at 175°C. Parylene-C is deposited with the substrate held at room temperature and exhibits

Symbol	**Parameter**	**Value**	**Units**
t	thickness	52	μm
d31	Piezo Strain Constant	23	$\frac{m/m}{V/m}$
d33	Piezo Strain Constant	-33	$\frac{m/m}{V/m}$
ϵ	Relative Permitivity	12.0 to 12.8	N/A
	Breakdown Voltage	80	$MV/meter$, DC, @25°C

Table 2.1: Properties of PVDF film

outstanding electrical isolation and is able to tolerate high strains. The room temperature deposition eliminates the risk of PVDF phase conversion and also deposits the material with no built in strain due to thermal expansion mismatch. This layer serves as the gate dielectric layer of the transistors and also planarizes the PVDF surface, which is rough due to the stretching process used to crystallize the sheet. This layer traps the generated charge on PVDF and prevents charge from leaking through the source or drain electrodes or into the charge channel. Patterning of this dielectric is not required for this structure.

40nm of gold was thermally deposited onto the dielectric layer and patterned photolithographically to form the source electrode and the drain electrode. Prebake and postbake at this step are under 80° Celsius to prevent exceeding the Curie point of the PVDF; 75°C was used. During the fabrication process, curling of the PVDF sheet is observed once the temperature exceeded 85°C. The curled sample cannot proceed to the next process. Also, this curling is not reversible once the sample is deformed by heat. The source and drain mask was designed with a W/L of 200 for this project. All the contacts were extended to the bottom of the sheet and connected via a flex circuit to a printed circuit board that interfaced to a switch matrix (Keithley 7001) and dual channel source measurement unit (Keithley 2602). This arrangement was used to measure the I-V characteristics and the source/drain current response for all of the transistors.

In order to shift the threshold voltage of the organic transistor and have the transistors operating at linear region, 20 seconds of UV-Ozone exposure was used to treat the dielectric layer after the source/drain electrodes are defined. Shifting the threshold voltage forces the transistor to operate in the linear region, increases source/drain current magnitude, and permits bipolar operation by preventing the device from entering cutoff when a positive gate voltage is applied by the piezoelectric, allowing operation in both tension and compression. [**?**]

25nm of pentacene was then thermally deposited at a rate of one angstrom per second with the substrate held at room temperature in a high vacuum environment. Final encapsulation was performed by coating with 200nm of parylene-C to protect the active layer from water and air.

2.4 Characterization and measurement

2.4.1 Measurement setup

The final structure which has a four by ten sensor array (as shown in Fig. 2.3) serves as a surface strain sensor. The size of a PVDF substrate is 5cm by 5cm; PVDF generates charge in response to strain at each location, and this charge provides the gate voltage of the OFET which induces a channel in the active layer and turns on the transistor. To increase the strain and create a more repeatable deformation, the PVDF film was laminated to a 0.8mm thick PVC card. The PVDF film is thin and mechanically compliant. Lamination to the

PVC card tensions the PVDF by displacing it from the neutral deformation plane. A robotic actuator was used to reproducibly displace the card. The back reference electrode was connected to the source electrode and grounded. The equivalent circuit of a single strain sensor element is shown in Fig. 2.1.

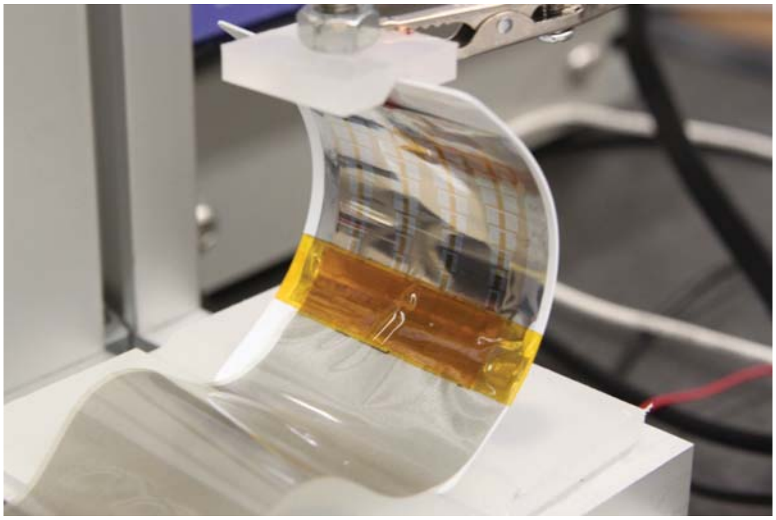

Figure 2.3: The completed 4 X 10 strain sensor array on PVDF substrate laminated to a PVC card. A printed circuit board interfaces the finalized device to the measurement apparatus. A robotic actuator deformed the PVC card from it neutral plane; and the current of all forty OFETs integrated with the PVDF film can be measured to map the strain field of the PVC card.

Bias was applied between source and drain by the Keithley 2602 source meter. The source/drain current was measured over time. During the measurement, the actuator first deformed the PVDF film, generating a gate voltage for the transistors. Then, the actuator released the PVDF film to its neutral position. This cycle was repeated for at least two times in a measurement.

2.4.2 Single device characterization

Fig. 2.4(a) shows the results of current measurement over 240 seconds. The sample was at its neutral position at the beginning, and the actuation started at the 50th second, then released back to the neutral position at the 100th second. The same operation was repeated at the 150th second and the 200th second.

The initial current is not zero because of the more positively shifted threshold voltage due to the UV-Ozone treatment and the induced dipole in the dielectric layer [**?**]. During the mechanical actuation, a large capacitive current due to the capacitance between the back reference electrode and the source/drain electrodes and interconnect is observed. After this actuation is completed, the current stabilizes, and is at a magnitude increased or decreased by the effect of the charge on the piezoelectric material on the channel. By comparing the current before and after the mechanical actuation and by applying the results to the transistor model, it is possible to determine the amount of charge generated by the piezoelectric polymer and calculate the strain directly underneath the semiconductor island. Because the piezoelectric material is directly coupled to the transistor channel, there is no capacitive divider with the gate-source and gate-drain parasitic capacitance and the charge on the piezoelectric can be directly determined independent of any parasitic effects in steady state. The effective voltage ratio of the parylene layer to the PVDF layer can be determined as a series connected capacitor stack:

$$Q = C \cdot V \tag{2.1}$$

$$Q_{PVDF} = Q_{Parylene} \tag{2.2}$$

$$\frac{V_{Parylene}}{V_{PVDF}} = \frac{C_{PVDF}}{C_{Parylene}} = \frac{\epsilon_{PVDF}/thickness_{PVDF}}{\epsilon_{Parylene}/thickness_{Parylene}} \tag{2.3}$$

$$\rightarrow \frac{12/52\mu m}{2/320nm} = 0.04615$$

Fig. 2.4(b) shows the current level versus time under both compressive and tensile deformation, demonstrating the effectiveness of this architecture in measuring a bipolar effective gate charge. This behavior is enabled by the UV-Ozone treatment and positive threshold voltage of the device. In this figure, the measurement was conducted after the sample was exposed to air for some time, so the current level was not as large as the previous figure due to the degeneration of pentacene. The degeneration can be improved by a better encapsulation.

2.4.3 Power consumption

The OFETs on the PVDF substrate are on at all times due to the shifted threshold voltage. The power consumption of a single sensor element at its neutral position can be estimated as:

$Idling\ Power = Idrain \times Vdrain = 0.1\mu A \times 35V = 3.5\mu W$

$Total\ Idling\ Power = Idrain \times Vdrain \times 40 = 0.1\mu A \times 35V \times 40 = 140\mu W$

When the device is deformed, the total power consumption depends on the level and the shape of the deformation. A higher power consumption will happen when more devices are operating at higher current level, and some decrease in power will be seen for deformations that decrease the current.

2.4.4 Control transistor - OFET on PVDF substrate with 20sec UV-Ozone treatment

A control transistor with a metal gate was prepared and characterized to determine the voltage generated on the PVDF (I-V curve is shown in Fig. 2.5).

The width to length ratio is 200 (W=3000μm, L=15μm), and the threshold voltage is -5V (this is shifted more positive relative to a non-UV treated control). We can compare the measured current from the strain sensor (Fig. 2.4(a)) to the current in the Id-Vg graph of the control transistor (Fig. 2.5 (b)) to estimate the voltage generated by the PVDF film. Nonlinear fitting was performed before comparing the source/drain current of the strain sensor and the control transistor. The initial current of 0.1μA corresponds to -8V of effective gate voltage; the peak current right after actuation is equivalent to -13V of gate voltage; the stabilized current level is equivalent to -9.5V applied gate voltage.

The result shows that organic transistors on PVDF film can be turned on by the gate voltage which comes from the induced charge on the PVDF film right after the deformation. A channel is formed by holes in the active layer which then conduct the carriers between source and drain. This current overcomes any capacitance in the interconnect given enough time to discharge and reach steady state.

2.4.5 Strain field mapping

We can use the difference between the current level after the actuation and the current level of the neutral position to reconstruct the strain field on the attached surface. There are 10 sensing devices on each column and four columns in total on the PVC card on which the mapping was performed. Devices are numbered from top to bottom on the Y-axis(1 to 10), left to right on the X-axis(0 to 4). Fig. 2.6(a) shows the result of the current change profile along the Y-axis when the card is bended as the picture shows, Fig. 2.6(b) shows the current change contour map when the card has a concentrated stain on the lower right side, and Fig. 2.6(c) shows the current change contour map when the card is twisted. The conversion of the current change to the actual strain level can easily be done by using Fig.2.8, which is explained in the next section.

2.4.6 Characterization of sensitivity

The sensitivity of the PVDF strain sensor is tested and compared with a commercial resistive strain gage (OMEGA precision strain gage SGD-1.5/120M-LY13) placed at the same location as the PVDF-OFET strain sensor. The cycles of displacement applied by the robotic actuator to the PVC card to which the PVDF strain sensor and the commercial strain gage were attached ranges from 0.001 inch to 0.8 inch, which corresponds to a force from 0.005 Newton to 2.1 Newton. The PVDF strain sensor has a source/drain bias of -35V; and the commercial strain gage is biased at 2V. Fig.2.7 shows the resistance of the commercial strain gage which has a initial resistance value of 120 Ohm and the source/drain current of the PVDF strain sensor versus elapsed time when three cycles of deformation were applied. The two curves have simultaneous response to the slowly applied stress (the actuator moved down and pressed the sample at 2 inch/min). The three cycles have a consistent shape which demonstrates the reproducibility of the PVDF strain sensor. Fig.2.8shows the current change of the PVDF strain sensor versus the strain derived from the resistance change of the commercial strain gage. Three cycles of press and release have repeatable results; however, during the release, a hysteresis is observed due to charge relaxation. This curve provides the conversion between the measured PVDF strain sensor current change and the actual strain of the attached substrate. A sensitivity of 0.182μA/strain(in percentage) can be estimated from Fig.2.8

The transistor is at ON-state at all time, so the source/drain current changes as long as the PVDF substrate generates piezoelectric signal. The speed limit is primarily dominated by the parasitic capacitance; therefore, when characterizing the sensitivity, slow actuation was applied to the PVDF strain sensor in order to rule out the influence of parasitics. The PVDF strain sensor was deformed from 0 strain to 2 percent strain in 30 second; and nearly no parasitic response was observed at this speed.

2.4.7 Charge retention time

A Keithley 2602 source meter, which has an input impedance larger than 10GΩ, was used to estimate the gate charge retention time. The PVDF strain sensor is biased at -35V on the drain end, and a 2 percent strain is applied to the sensor at a relatively fast speed. The current level of the PVDF strain sensor before and after the actuation is recorded to estimate the retention time of the generated piezoelectric charge. Measurement result is shown in Fig. 2.9. A time versus transistor current measurement is conducted in which the sample was deformed at the 50th second after the beginning of the measurement. We observed that the current level after the deformation discharges following a first order characteristic with a time constant of 442 seconds. The is a benefit of the metal gate-free configuration; without a metal gate, a single defect does not rapidly discharge the whole gate charge under actuation. The first stage of recovery is due to the parasitic capacitances that the device is seeing; while the second stage of the recovery is a result of relaxation and the defects in the dielectric layer (parylene-C).

2.5 OLED integrated strain sensor

Organic light emitting diode (OLED) can be integrated to visualize the stress/stain level. The PVDF strain sensor outputs current signal when it is compressed or tensioned, thus the current can be used to drive an OLED. The W/L ratio of the OFET on PVDF was designed to be higher than 2000 in order to have sufficient current ($\sim 1.5\mu$A)to turn on the integrated OLED. Fig. 2.10 shows the proposed structure and the actual sample for this demonstration. When the sample is deformed, OLED turns on and goes brighter if the deformation increases due to the amplified current of OFET. However, the turned-on OLED is more observable in a dark environment due to its current level. The OLED lights up and its brightness is proportional to the level of deformation. Fig. 2.12 shows the deformed sample in a normal background and the turned-on OLED due to the deformation in a dark background. The tail of the OLED image was due to the motion of deforming.

2.6 Conclusion of the chapter

The concept of using OFETs monolithically integrated on freestanding PVDF sheets to sense strain or stress has been demonstrated. The transistors form a transimpedance amplifier directly at each sensing site, allowing conversion of the piezoelectric charge signal into a current signal which can be externally detected. The transistors are treated using a process which shifts the threshold voltage positive, allowing bipolar measurement of the applied strain. A metal gate-free architecture is also used, which allows for a reasonable charge retention time following actuation.

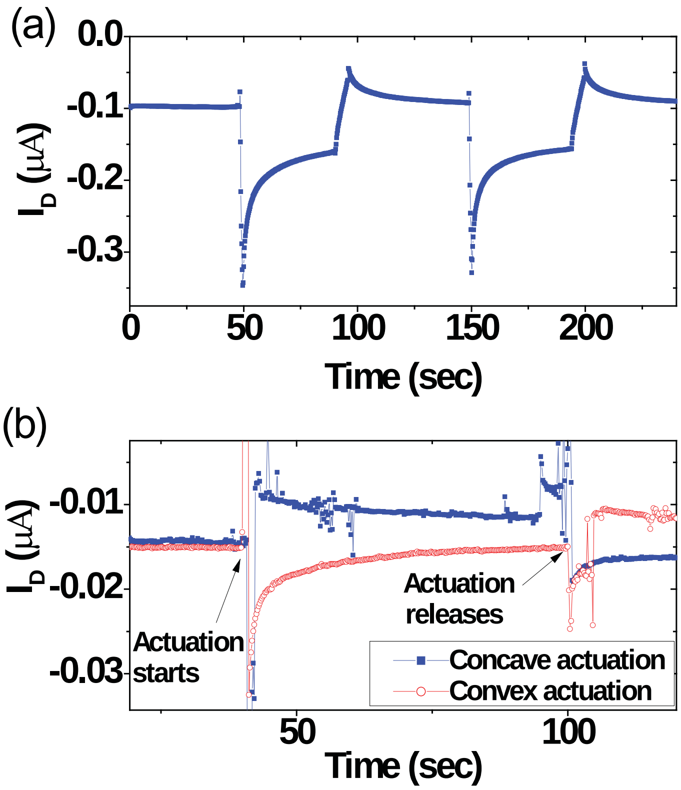

Figure 2.4: (a) The measured source-drain current for a single device at V_{DS}=35V. The device is actuated at T = 50s and T = 150s, and is released at T = 100s and T = 200s. The time step is 200msec. (b) The source-drain current at V_{DS}=35V under different direction of deformation. When the sensor is actuated with a concave shape (compressive strain), the current level was decreased. While under convex actuation (tensile strain) of deformation, the current level was increased. This bipolar sensitivity is enabled by the more positively shifted threshold voltage, which prevents the transistor from entering the cut-off region.

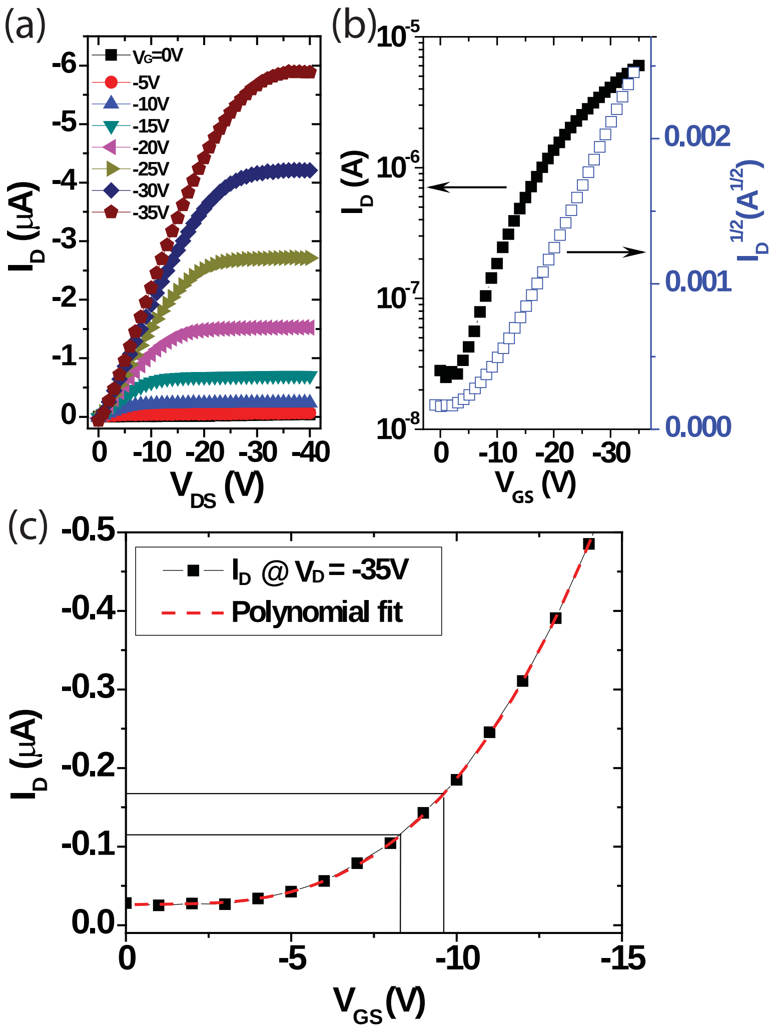

Figure 2.5: (a) $I_D - V_{DS}$ curve of control transistor with 20 second UV-Ozone treatment. A control transistor is a transistor with metal gate, and it is fabricated directly on the PVDF substrate. UV-Ozone is applied to shift its threshold voltage. (b) $I_D - V_{GS}$ curve of the control transistor with 20 second UV-Ozone treatment. (c) Square root scale and log scale of $I_D - V_{GS}$ curve of the control transistor.

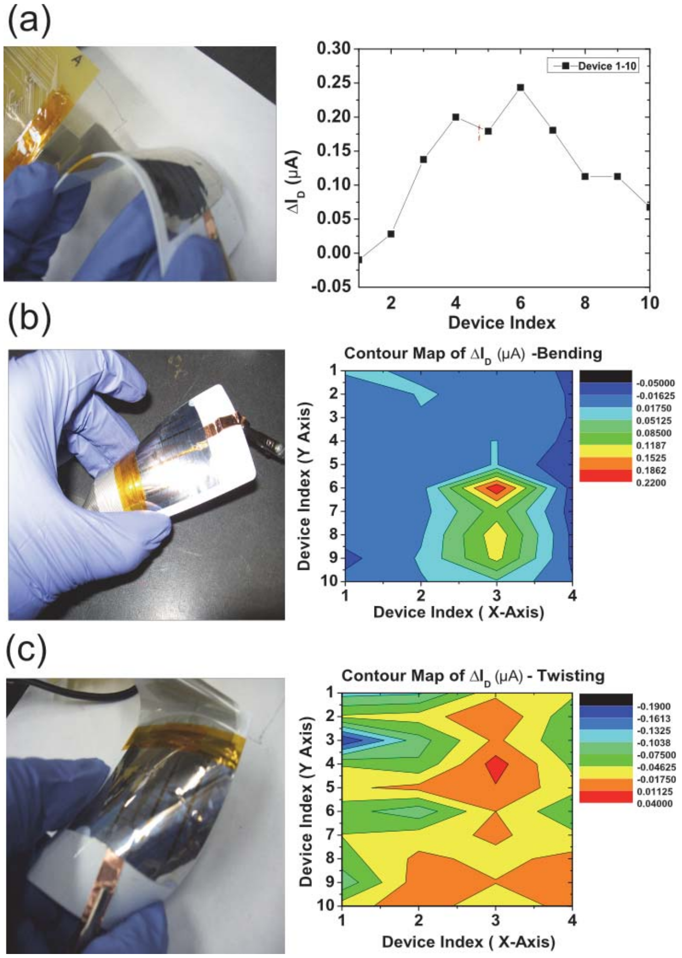

Figure 2.6: (a) 1-D Strain field mapping of a bent strain sensor attached to a plastic card on the Y-axis (longitudinal), showing the trend of the local strain. (b) 2-D Strain field mapping of a deformed strain sensor at the lower bottom area. The 2-D contour map indicates that at the middle bottom part of the plastic card, strain is more concentrated. (c) 2-D Strain field mapping of a twisted strain sensor. The 2-D contour map shows an oblique strain concentration that complies with the shape of the twisting.

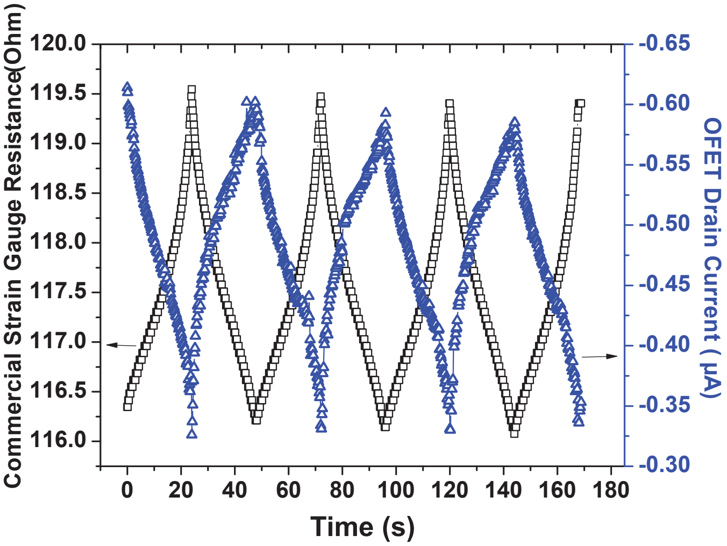

Figure 2.7: Resistance of the OMEGA precision strain gage and the measured current of the PVDF strain sensor versus time. Three cycles of press and release at a speed of 2 inch/min from 0.001 inch to 0.8 inch in 240 seconds are applied to the testing sample. The two sensors are located at the same location on the PVC substrate but on different faces. The commercial strain sensor has been tested and proved to have the same response to compressed and tensile stress, so it is attached to the opposite face of the PVDF strain sensor to provide the actual strain level for reference. Note that a initial displacement of 0.001 inch is used to ensure the three cycles of measurement have the same direction of deformation.

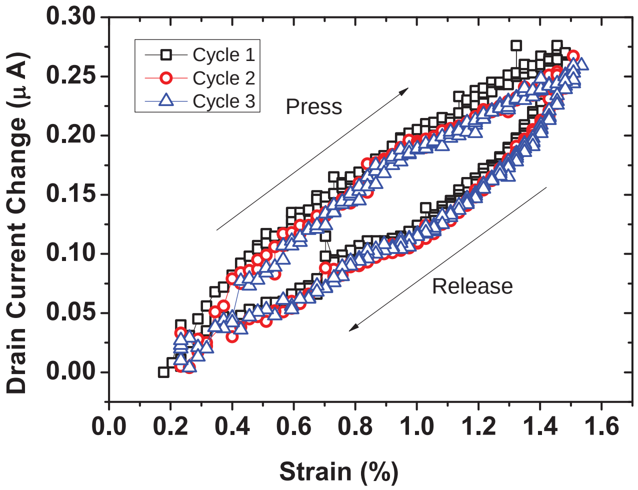

Figure 2.8: Current change of the PVDF strain sensor versus actual strain level derived from the resistance change of the commercial strain gage. Three cycles of press and release are applied to the testing sample, and each cycle deforms the sample from 0.001 inch to 0.8 inch and back to 0.001 inch at a speed of 2 inch/min. A hysteresis during the release section of actuation is observed mainly due to the piezoelectric material charge relaxation.

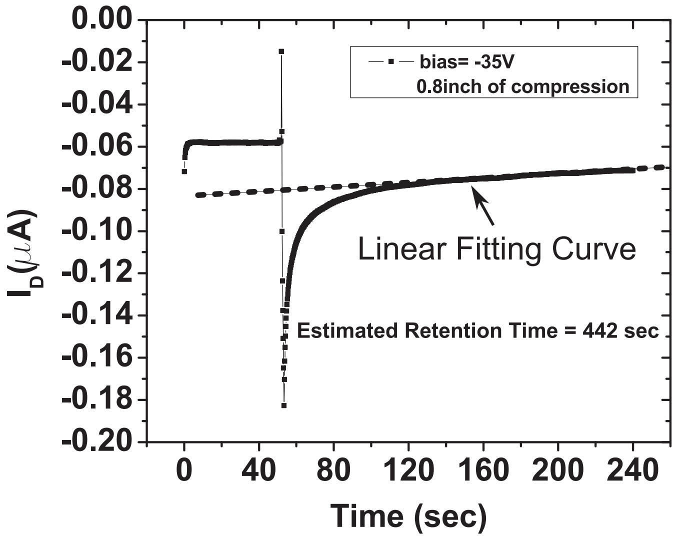

Figure 2.9: I_D as a function of time, demonstrating gate charge retention. The gate charge follows a first order decay, and a tangent is shown as a guide to estimate the characteristic retention time. Actuation began at $T = 50$s, and 442 seconds of retention time was estimated through linear fitting of I_D.

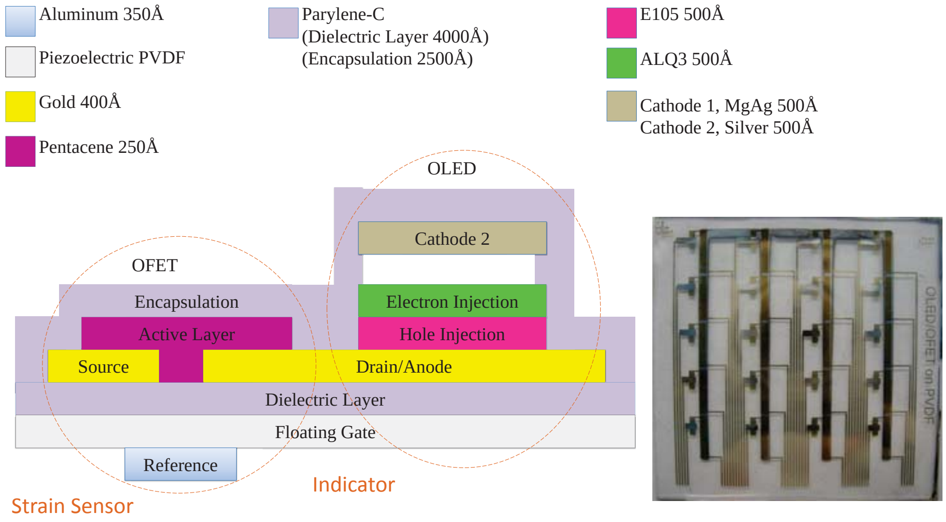

Figure 2.10: OLED integrated with strain sensor.

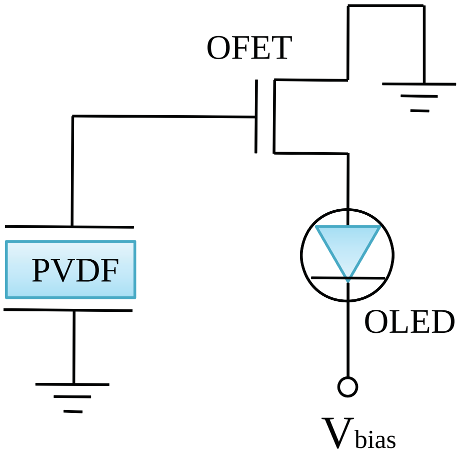

Figure 2.11: The equivalent circuit of OLED integrated strain sensor.

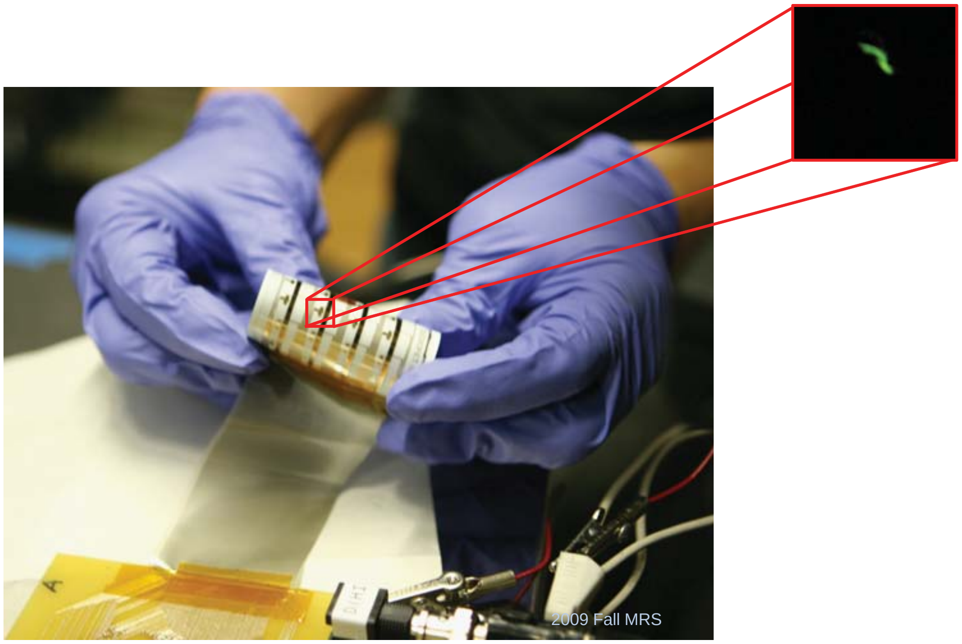

Figure 2.12: The picture of OLED integrated strain sensor.

Chapter 3

Tone Analyzer

3.1 Introduction

The vibration and propagation of air induce a marvelous phenomenon - Sound. Analyzing the frequency of sound with a simple device has been an interesting topic, and this interest has grown larger as people foresee the need from portable telecommunication device, human-like robot, and hearing-aid instruments. Therefore, A device that can contribute to the hearing ability of human and even human-alike droid in the near future, that employs the beauty of material nature, and that is simple and low-cost for mass reproduction is one of the ultimate goals in the area of sound device research and development.

Instrumenting resonant acoustic structures makes it possible to implement mechanical signal processing functions that can localize sound and determine its frequency composition. Perhaps the most elegant mechanical signal processing system is the cochlea, which is a distributed resonator that converts the frequency composition of sound into a specific pattern of mechanical motion. The mechanism of operation of the mammalian cochlea was clearly illustrated by Wilkinson et al.[?]. Wilkinson proposed, and subsequent experiments have confirmed, that the triangular cochlear shape has a displacement peak at a different position for different frequencies of sound. Specialized nerve cells are stimulated by the chochlea's displacement and the brain can analyze the frequency of incoming sound by determining the locations of greatest mechanical displacement along the chochlea's length instead of performing time-domain determinations of the incoming sound spectral composition. [?] [?] Silicon based micromachined biomimetic sensors that use the geometry and concept of cochlea have also been successfully fabricated. [?]

Knowing that the vibration pattern of a triangular film-like resonator connects to its reactions to the frequency of sound, a direct detection of the vibration pattern is thus viable to be used to determine the sound frequency. One of the most direct method is to use a pressure-sensitive material to form the resonator. Piezoelectric polymer is a strong candidate for this application for its extraordinary properties on this type of application.

The piezoelectric and ferroelectric properties of polyvinylidene difluoride (PVDF) was first discovered by Kawai. [?] [?] Piezoelectric polymers such as PVDF have a number of advantages over ceramic piezoelectrics in many acoustic applications including a high achievable peak strain, [?] conformability to flexible surfaces, [?] and a better acoustic impedance match to water and most plastics than ceramic piezoelectric elements. [?] It is these properties that make PVDF acoustic microphones and actuators well suited for ultrasonic imaging in biological and sonar systems. [?]

Because of their flexibility and conformability, several array sensors using piezoelectric polymer materials have been developed to map strain and pressure on surfaces. Reston, et al. [?] and Kolesar, et al. [?] have demonstrated a pressure sensitive array sensor fabricated by laminating a layer of PVDF onto an rigid array of silicon field effect transistors integrated with amplification circuitry. Stadlober et al. demonstrate sensing both through use of a piezo/pyroelectric gate dielectric and a hybrid attached sensing element to an organic field effect transistor (OFET). [?] Other flexible sensors have also been developed to map low frequency pressure on surfaces, for example, the active matrix mechanically flexible pressure sensor demonstrated by Someya et al. which uses a conductor loaded elastomer whose resistance changes with applied pressure. [?] Sound detection and analysis using piezoelectric materials has been demonstrated by a number of groups for a range of applications including construction of microphones and implementing mechanical signal processing. An electrooptic polymer-based acoustic spectrum analyzer, for example, has been demonstrated to have a wide bandwidth and high frequency resolution. [?] A MEMS-based acoustic filter proposed by Li, et al. exhibits near zero-loss and a extremely short response time. [?] A micropillar based device presented by Xu, et al. shows that the footprint of piezoelectric devices can be small while retaining high sensitivity. [?] [?]

We are proposing a tone analyzer based on distributed resonators made using a tensioned sheet of PVDF that implements a mechanical signal processing function analogous to that (but using a different mechanism) that of the cochlea. The tensioned piezoelectric sheet converts mechanical movement into a repeatable and measurable charge signal pattern, and sensors built on the sheet enable direct detection and determination of sound frequency composition without the need for time-domain electronic signal processing of the incoming signal. This system takes advantage of linearity and builds a pre-measured signal pattern database for matching the resonant modes to the resonator excitation shape. We further integrate organic field effect transistors (OFETs) with the PVDF to form transimpedance amplifiers that convert and amplify the charge signal generated from PVDF sheet to a more useful current signal without mechanically loading the system. The fabrication process is simple enough so that its integration into another system will be relatively easy. Also, the computation of excitation frequency uses an algorithm that is uncomplicated for any existing computer system.

3.2 Device design & Fabrication

3.2.1 Distributed capacitor array type of tone analyzer

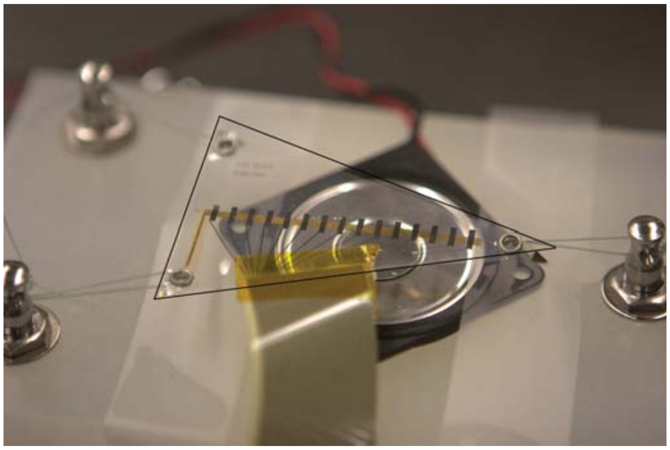

Figure 3.1: The distributed capacitor array type tone analyzer. Fifteen top electrodes (aluminum) are patterned on the material opposite a common reference electrode (gold) on the other side of the piezoelectric sheet. A speaker is mounted underneath the device to excite the device. The white plastic rack uses three guitar tuners in order to tension the device. A low-stretch fishing line is used to apply tension to the resonator. The outline of the PVDF sheet been highlighted with a black line.

Table 3.1: Properties of PVDF sheet

Symbol	**Parameter**	**Value**	**Units**
t	thickness	52	μm
d_{31}	piezo constant	23×10^{-12}	C/N
d_{33}	piezo constant	-33×10^{-12}	C/N
ϵ	relative permitivity	12	–
–	breakdown voltage	~ 80	MV/m, DC @25°C

The first design implemented is a distributed, directly addressed piezoelectric sensor structure, which is shown is Fig. 3.1. The sheet is shaped in a triangle, to create a fusion of its modal shapes, and the size is selected to allow the observation of modes in the acoustic frequency range. 15 sensors are used to adapt the piezoelectric sheet and measure the deformation pattern that occurs when a different frequency of incoming sound excites the piezoelectric material. The PVDF material used was supplied by Measurement Specialties, Inc. Some important properties extracted from Table 1.1 are listed in Table 3.1.

3.2.2 Integrated organic transistor tone analyzer

As we finished the distributed capacitor array type of tone analyzer, we have come to realize that having the charge signal converted to a more measurable current signal can create a better potential for any future integration with other devices. It is straightforward that the advanced version of PVDF tone analyzer would require a transimpedance amplifier to convert the charge signal. However, the PVDF sheet has a low Curie temperature of 80°C [**?**], which made silicon technology unsuitable due to it high process temperature. Organic thin film transistor, on the other hand, can be fabricated and processed in room-temperature and possesses mechanical flexibility. Thus, choosing OFETs to integrate with PVDF by using a monolithic architecture became the main focus of our second tone analyzer design. [**?**] This design offers more flexibility for future applications such as array deployment, where the signal collected from the piezoelectric polymer needs to be converted and amplified in the face of significant parasitic capacitance.

The second design implemented integrating OFET-based transimpedance amplifiers at the fifteen sensing sites, and the fifteen sensing sites on the piezoelectric sheet measured the deformation pattern that occurs when different frequencies of sound excite the sheet. The transistors are depletion mode devices, which are tuned to be in the on-state at $V_{GS} = 0V$ using a UV-ozone treatment, [**?**]to increase the sensitivity to the charge generated from the motion of the piezoelectric sheet and lend bipolar behavior to the device.

The finalized implementation of this design is shown Fig. 3.2. Fifteen devices along the triangular device map out the mechanical movement pattern, which can be measured as an AC current. The map of this current provides the data used to build the response matrix for the analysis of incoming sound frequencies.

3.2.3 Fabrication process

To fabricate the distributed capacitor array type of tone analyzer, a 52μm-thick pre-poled PVDF sheet material was used as the substrate and the main sensing element. To begin the substrate preparation, the PVDF sheet is cut into a 3.5cm in width and 6.2cm in height triangle. 50nm of aluminum was then thermally deposited on the top surface of the PVDF sheet and lithographically patterned into fifteen pad electrodes with a fanout for a heat seal connector. 40nm of gold was thermally deposited on the back of the PVDF sheet and patterned to form the common electrode. This process is shown in Fig. 3.3 as Architecture I.

The integrated organic transistor type requires two more steps than the capacitor array structure. A layer of parylene-C (dix-C, Uniglobe Kisco, 250nm) was deposited using a room temperature CVD process after the triangular shape of the PVDF sheet was cut out. The PVDF sheet was stretched during the poling process, thus the surface roughness is too high for the formation of organic thin film transistors. This parylene-C layer smooths the PVDF surface for the subsequent organic semiconductor deposition. 40nm of gold was then thermally deposited on top of the parylene-C layer and patterned to form the source and the drain electrodes for the transistor. On the opposite face of the PVDF sheet, 50nm of aluminum was deposited and patterned to form a common electrode. Finally, 25nm of pentacene was deposited and encapsulated with another layer of parylene-C on the top surface of the sheet. This process is shown in Fig. 3.3 as Architecture II.

3.3 Characterization and measurement

3.3.1 Measurement setup

Three holes were punched in the finished tone analyzer sheet and were reinforced with metal eyelets. The eyelets were threaded with a low stretch 330 micron fishing line (Berkley Trilene) to tension the sample during the measurements. The device was tensioned using three guitar tuners mounted on a plastic platform. This tensioned tone analyzer made of triangular sheet of PVDF converts physical movement caused by acoustic pressure wave into a charge signal due to its piezoelectric nature. This distributed resonator was instrumented with a series of 15 distributed piezoelectric sensors, and the characteristic modal patterns can be determined experimentally. These modal patterns can then be matched to the known modes of the resonator and the spectral composition of the incoming acoustic signal can be directly determined without the need for time-domain analysis. A speaker was mounted on the rack directly underneath the device to excite the PVDF sheet. This setup was used to test both designs, and they are shown in Fig. 3.1 and Fig. 3.2.

The piezoelectric response of the resonator was measured using a current amplifier and a lock-in amplifier (Stanford Research, SR-830) synchronized to the excitation reference frequency from a function generator. In architecture I, the distributed capacitors would be charged by the piezoelectric film, thus we were measuring an AC capacitive current signal. In architecture II, the charge generated by the piezoelectric sheet was converted into transistor current, therefore thee transistor AC current was expected to be measured. The absolute magnitude of the response at each location on the PVDF sheet was measured and recorded. A switch matrix arrangement (Keithley 7001) allowed for automated data collection from each site.

3.3.2 Full range scan

The tension level and the geometry of the triangular PVDF sheet determine the response pattern. A wide frequency scan was first performed to find the overall resonant frequency range of the specific design and tension settings. The higher response frequency range scan is shown in Fig. 3.4. The measurement was then re-focused on the frequency range with a larger response, which ranges from 500Hz to 1500Hz.

3.3.3 The response matrix

A response matrix was formed by measuring the devices at 15 random non-harmonic frequencies within the higher response range. Fig. 3.5 shows the measurements at 827Hz using the distributed capacitor array architecture. The measurements were repeated for ten times at the fifteen chosen frequencies to ensure that the measured data are reproducible. These were then averaged to form the response matrix. Sound frequency versus signal measurements were also conducted using the integrated organic transistor tone analyzer architecture. The results of two of the fifteen chosen frequencies are shown in Fig. 3.6. The characteristic peak responses are at different sites, and we can use their identities in terms of amplitude and shape to form the 15x15 response matrix.

The fifteen non-harmonic frequency responses over the fifteen sensor sites are arranged in a 15x15 response matrix R. Fig. 3.7 shows the fifteen response functions of the of the distributed capacitor array type tone analyzer, where it can be seen that each of the 15 frequencies has a unique amplitude and shape. This response matrix contains the information for conversion between the mechanical signal processing performed by the distributed resonator structure and the frequency domain acoustic composition, and it is the key measurement result for the analysis of sound frequency.

3.3.4 Deriving excitation frequency

We define the measured current response of an incoming sound at 15 different sensor sites as the measured signal vector ($\vec{M}$), and the vector that connects the 15x15 response matrix and the response vector as the excitation vector ($\vec{E}$). The excitation vector can be seen as a weight function the relates the measured current response to the previously measured response database. Since $\vec{M} = R \times \vec{E}$:

$$R^{-1} \times R \times \vec{E} \;\; = \;\; R^{-1} \times \vec{M} \tag{3.1}$$

To experimentally demonstrate this frequency detection concept, the current response vector at 827Hz of the distributed capacitor array style tone analyzer was measured again after the response matrix R was constructed, and the measured signal vector $\vec{M}$ was multiplied by the inverse response matrix R^{-1}. We obtained an excitation vector $\vec{E}$. The derived excitation vector showed that the eighth frequency component in Fig. 3.8 has the highest weight, indicating that the measured response vector resembles the eighth frequency component most and has the best match to its amplitude and shape. The eighth frequency component in the response matrix (Fig. 3.7) can be found to be 827Hz , thus the external sound excitation frequency to the PVDF tone analyzer was 827Hz could be concluded.

3.4 Conclusion of the chapter

A tone analyzer was produced by using a sheet of a piezoelectric polymer material both with and without the transimpedance amplifier (organic thin film transistors). The directly addressed array type, a simple architecture without integrating with organic transistors, proves the concept of producing a distributed resonator with frequency dependent modal response. The integrated organic transistor strain sensor type, a variant of the distributed capacitor array type with transimpedance amplifiers, shows the capability of detecting sound frequency and opens more possibilities for more sophisticated application that can benefit from a amplified current signal. The use of piezoelectric sheet material to determine frequency composition of a single tone by matching the response shape without using any time domain (e.g. FFT) analysis is demonstrated.

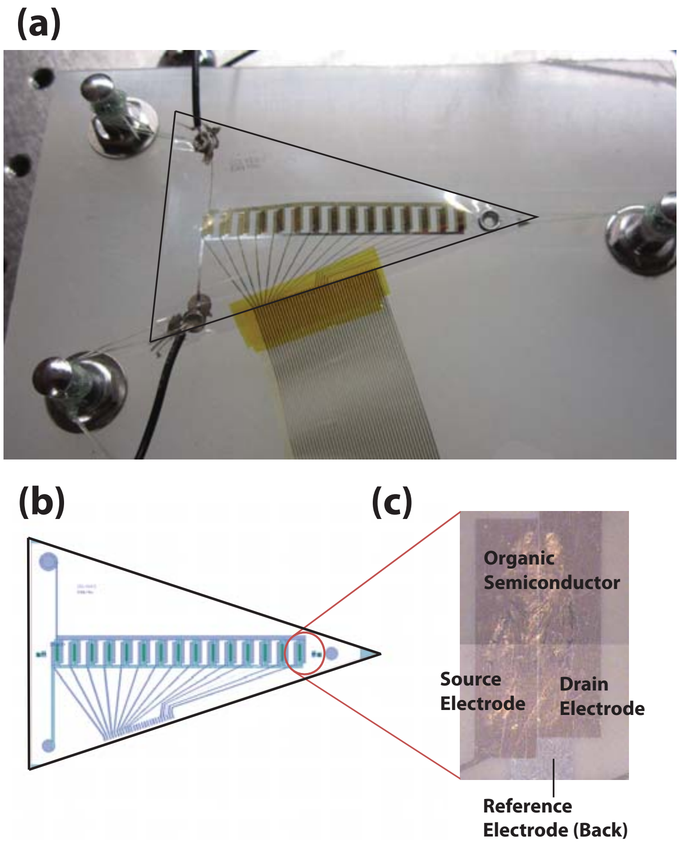

Figure 3.2: (a) Integrated organic transistor tone analyzer. Fifteen transistors are patterned on the PVDF sheet, opposite a common reference electrode (aluminum) on the opposite side of the piezo sheet. A speaker is used to excite the device. The white plastic rack uses three guitar tuners and low tension fishing line to tension the device at three points. The outline of the PVDF sheet been highlighted with a black line. (b) The design of the integrated organic transistor tone analyzer. (c) A single sensor element. The channel length of the transistor is 20μm, and the channel width is 3700 μm.

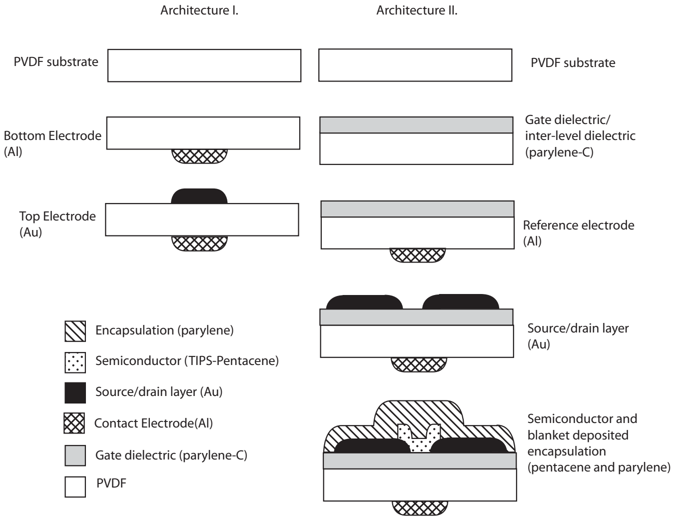

Figure 3.3: (a) Architecture I: Fabrication process of the distributed capacitor array type tone analyzer. (b) Architecture II: Fabrication process of the integrated organic transistor tone analyzer.

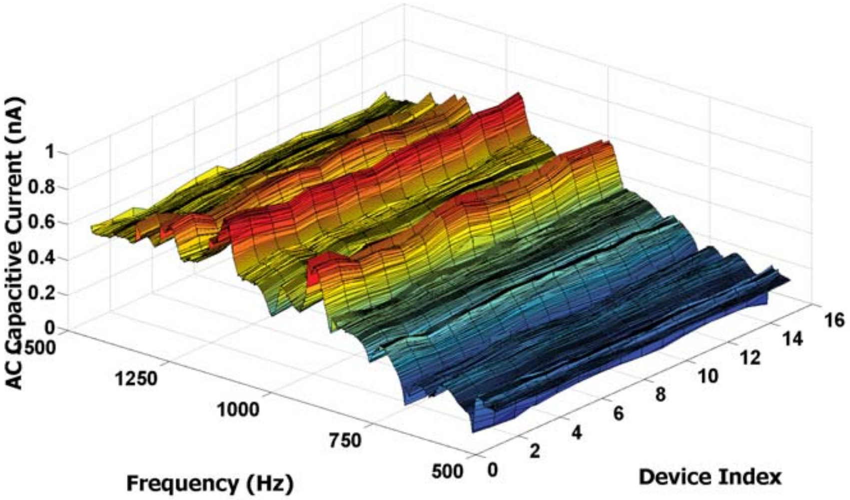

Figure 3.4: A measurement site (device)/frequency/current plot. The X-axis is the piezoelectric sensor device index. These are counted from 1 to 15, 1 is at the wide part of the triangle and 15 is at the tip. The Y-axis is the excitation frequency in Hertz, and the Z-axis is the amplitude of the measured piezoelectric response.

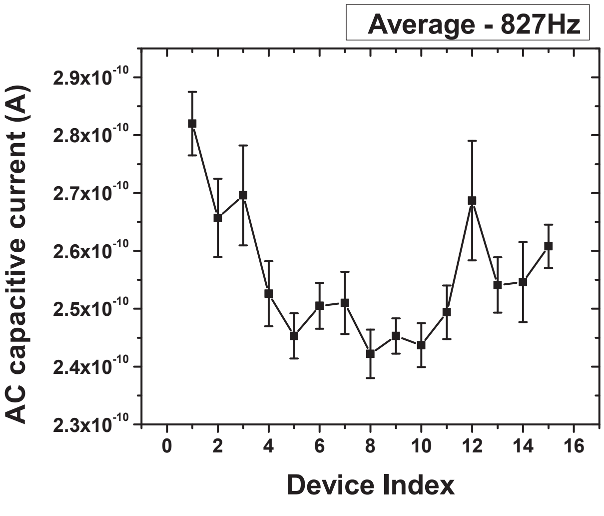

Figure 3.5: The measured AC piezoelectric response at 827Hz using the distributed capacitor array architecture. The average curve will be used to form the response matrix.

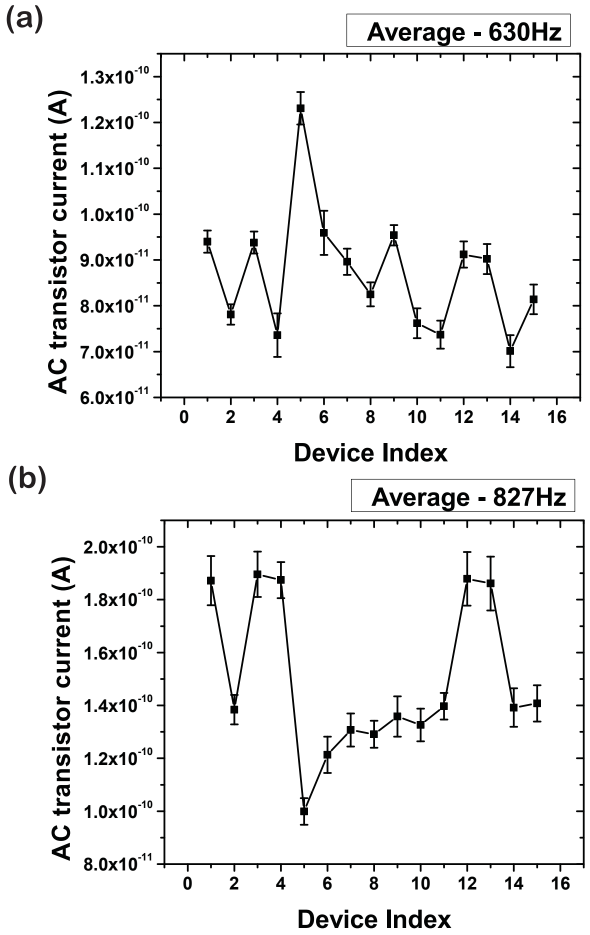

Figure 3.6: (a) The measured AC transistor response current at 630Hz along the 15 sensor elements using the integrated organic transistor tone analyzer. (d) The measured AC transistor response current at 827Hz along the 15 sensor elements using the integrated organic transistor tone analyzer. Ten measurements were taken to insure repeatability, and the average value is used to construct the 15x15 response matrix. The error bars show the standard deviation for each set of repeated measurements in the set.

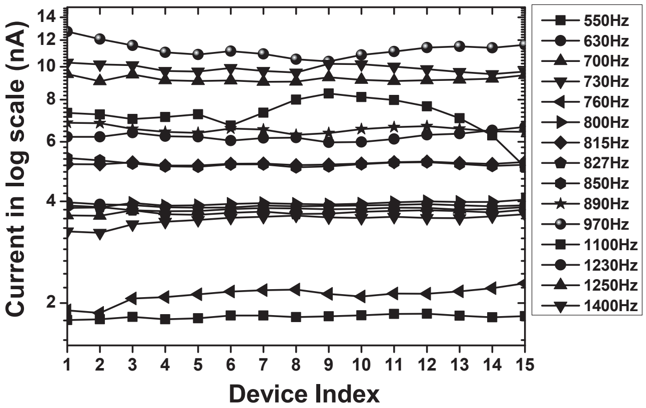

Figure 3.7: 15 curves of 15 random-picked non-harmonic frequencies with higher response versus the measured AC capacitive current at 15 sensing sites using the architecture of distributed capacitor are plotted. The 15x15 response matrix (R) is then formed by these fifteen curves. The responses are arranged from lower frequency to higher frequency (from top to bottom)in this graph.

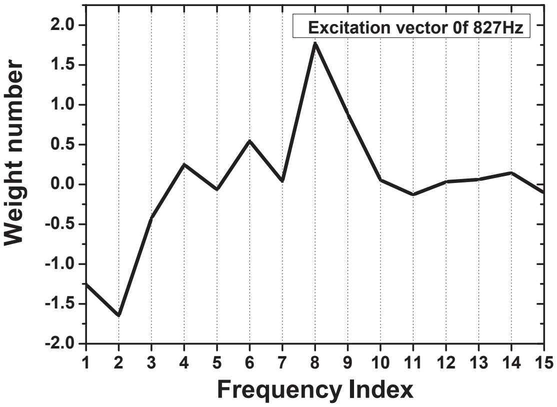

Figure 3.8: The derived excitation vector of 827Hz. we can see the eighth frequency component has the highest weight number, so we know this shape and amplitude fit the eighth frequency the most, which is 827Hz.

Chapter 4

Arrayed Microphone

4.1 Introduction

Capturing and visualizing sound fields has been a key technique for a variety of applications. This ”sound camera” snapshot allows engineers to design and diagnose using the captured sound field either emitted or reflected from the target object. Nondestructive testing, for example, benefits from sound field visualization to find any minor unwanted structural discontinuities through the reflection pattern of an incident testing sound wave. On the other hand, the strength profile of a sound field is equally valuable for some other applications such as the estimation of noise level from large transportation carriers. The visualization of sound level distribution helps the engineers to refine their design in terms of reducing the noise by controlling the streamline and arranging and placing the parts that generate higher noise properly. Arrayed microphone, as one of the most intuitive solutions for sound field visualization, can even be more useful in many other aspects. For instance, the principles of acoustical holography rely on microphone array to carry out its full functionality [?], and a directional listening device is made possible by adopting microphone array on a mobile robot [?]. Even ultrasonic imaging [?] and boundary layer turbulence measurement [?] are the benefiters of arrayed pressure sensors and microphone.

There have been a great amount of efforts on making arrayed microphones that can satisfy the specs and needs. Above all, having highly sensitive pressure sensors is the most critical foundation of building such an arrayed microphones system. These applications typically use sensing elements that are directly connected to the amplification and sense circuitry. Piezoelectric, piezoresistive, and other pressure-sensitive materials therefore become the very element of most of the pressure sensors and microphone. Graz et al. have demonstrated a concept of using ferroelectret field-effect transistor for pressure sensor and microphone [?]; an ultrasensitive piezoresistive organic thin film is craftily made by Laukhina et al. [?]; Flexible pressure sensors with microstructured rubber dielectric layers that can detect the weight and the footprint of a butterfly is showed by Mannsfeld et al. [?]; Someya et al. have created a stretchable pressure sensor network using pressure-sensitive rubber and organic thin film transistors for the skin application of a robot[?] These devices have really pushed the evolution of pressure sensors and microphone to a brand new era. Not only are large scale arrayed microphones needed for many applications, but also small scale arrayed microphones are craved by many engineers who are working in the field of structural engineering, biomedical engineering, and even telecommunication engineering. A trend of higher resolution and responsivity with a lower price is what this technology is moving toward. However, the complexies and cost have slowed down the progress of its development.

Two dimensional array utilizes the technologies mentioned above has been successfully developed, but how one can increase the resolution and decrease the complexity have become an difficult issue. An approach to increasing the number of sensing sites is to use array addressing of the individual sensing elements, allowing interconnect scaling to scale with the square root of the number of sensing sites. Two dimensional array designs using piezoelectric sensors require local amplification at the sensing site to overcome charge sharing through interconnect and switching parasitics.[?] [?] Hybrid silicon-based designs have been demonstrated for 2-D active matrix sensing systems, based on bulk and thinned crystalline silicon, but the bonding and substrate involved in these approaches can compromise the mechanical and acoustic properties of the sensors, as well as placing a limit on their ultimate size. [?] [?] [?]

A novel approach that we are proposing here is a direct and simple method which integrates piezoelectric sheet material and organic thin film transistors monolithically to form a transimpedance amplifier converting the charge signal from the piezoelectric sheet to a highly measurable current signal.

Piezoelectricity in polymers was first reported in polyvinylidene difluoride (PVDF) by Kawai in 1969. [?] Piezoelectric polymers present several advantages over ceramic piezoelectric materials for sensor applications; they exhibit greater mechanical flexibility, a larger survivable strain, a lower modulus, a better acoutstic impedance match to water, and higher charge generation per unit force over a wide bandwidth range. [?] These properties have driven the use of PVDF for a variety of single site and directly addressed and externally multiplexed array systems. [?] Despite these advantages, the development of a two dimensional array sensor system using PVDF presents several challenges. Charge generated at each sensing site is shared with downstream capacitive parasitics, and parasitic piezoelectric excitation can lead to crosstalk between sensed areas. We present an active matrix array of PVDF sensors with switching, allowing array addressing of individual elements, and local transimpedance amplification of the piezoelectric charge signal, overcoming attenuation of the charge signal by parasitic capacitance in the switch elements and interconnect. The architecture is engineered with low enough parasitic capacitances in the signal path to allow acoustic detection bandwidth. We use organic field effect transistors (OFETs) in this system to allow fabrication of the active circuitry required directly on crystallized and poled piezoelectric PVDF sheets without exceeding the thermal budget of the PVDF material, which has complicated hybrid and monolithic integration. [?]

4.2 Design

We designed an 8x8 matrix for this demonstration, and the sample is shown in Fig. 4.2. Each sensor element is controlled by an organic thin film transistor, we refer to this transistor as the switch transistor. The switch transistor is sized significantly smaller than the amplifying/sensing transistor to optimize the cell isolation, on/off characteristic, and parasitic load. The schematic of a single element which consists of a switch transistor and a sensor transistor is shown in Fig. 4.3. The sensor element converts the charge response of the PVDF into a current signal, overcoming downstream parasitic charge sharing from both switch transistors and interconnects. The equivalent circuit model is shown in Fig. 4.4.

To fabricate the OFETs, we used 6,13-bis(triisopropyl-silylethynyl) pentacene (TIPS-pentacene, Sigma-Aldrich), which is an air-stable organic p-type semiconductor. The integrated design of the sensor and amplifier eliminates an otherwise dominant parasitic capacitance between the gate and source/drain of the transimpedance amplifier, allowing an acoustic bandwidth response while retaining the thin and flexible form factor for maximum versatility in applications. In this work, the device was tested using both turbulent air current and far field acoustic excitation.

Our design uses pre-crystallized and pre-poled piezoelectric polyvinylidene difluoride (PVDF) which is commercially available. This material has a wide bandwidth, allowing application in broadband acoustic sensors. [?] [?] There have traditionally been two obstacles to the creation of high frequency PVDF 2-D matrixed array sensor devices: a large parasitic capacitance in thin film amplifiers, and parasitic piezoelectric coupling between interconnect elements. Our current design overcomes these limitations through local amplification and switching, while operating within the thermal budget presented by PVDF's low Curie point (∼80°C)[?]. The piezoelectric charge directly couples to the channel of the OFET, forming a localized transimpedance amplifier on the piezoelectric polymer built using low temperature (<60°C) organic field effect transistors. No metal gate is present, which increases the charge retention time and increases the effective bandwidth. [?] An OFET switch is also integrated in each unit cell, allowing switching of the output current using a small number of interconnect lines and preventing charge sharing from unaddressed elements. This structure allows the use of the arrayed piezoelectric polymer as an active matrix microphone.

4.3 Fabrication process

Pre-crystallized and pre-poled 52μm-thick PVDF film (provided by Measurement Specialties Inc.) is used as the substrate. Aluminum (100nm)is thermally evaporated and patterned to form the gate of the switch transistors, while the charge from the PVDF directly gates the sensor transistor. Parylene-C (200nm, Uniglobe Kisco dix-C) is deposited by CVD as the dielectric layer for both the switch transistors and sensor elements. Parylene-C also smooths the surface of the PVDF, allowing for better transistor performance. Gold (40nm) is thermally evaporated and patterned to form the source and drain electrodes. Another layer of aluminum (35nm) is deposited on the back of the PVDF substrate and patterned to serve as the reference electrode. The sample was treated with pentafluorobenzene thiol to improve the source/drain contact behavior. [?] [?] UV-Ozone treatment is applied to only the sensor transistors before the thermal evaporation of the active layer in order to shift the threshold voltage of the sensor transistor more positive.[?] TIPS-pentacene (25nm) was then thermally evaporated as the active semiconductor. [?] Parylene-C (250nm) was deposited as a final encapsulation layer. The process flow is summarized in Fig. 4.1.

4.4 Measurement and characterization

Keithley source meter (2400 and 2602), Keithley 7001 switch matrix, Agilent power supply are the major instruments for the measurements and characterization. The sample was contacted using a flex circuit and an anisotropic conducting adhesive. A thick PDMS block provided a compliant support for turbulence measurements, and the device was freestanding for speaker-based acoustic measurements. Sensitivity to turbulence, the localization of the acoustic response, and the response bandwidth were tested using a stream of compressed air from a 6mm-diameter tube. This measurement setup is shown in Fig. 4.5. The compressed air is controlled by an electric air valve, so that the measurement can be automated. The RMS current value was recorded by Keithley 2602 source meter for each element after the turn-on transient and is plotted onto a interpolated false-color map (Fig. 4.6). Keithley 7001 is used to select the device, and it also close and open all the channels between measurements to discharge the sample. This measurement demonstrates the signal localization. A time domain measurement of the current signal is shown in Fig. 4.7.

The time domain current signal (Fig. 4.7) and its Fourier Transform (Fig. 4.8 and Fig. 4.9) shows the bandwidth of the device extends to 15kHz. From this measurement, we have observed the signal localization and a frequency response covering a broadband acoustic range. The noise floor is shown in Fig. 4.8. This is a combination of room acoustic noise, measurement instruments noise, and noise from the switch transistors. The composition frequency and level is also analyzed (Fig. 4.9). The signal to noise ratio is estimated to be 100 to 1 by comparing Fig. 4.8 and Fig. 4.9, and then the signal to noise ratio reaches 1 when the frequency reaches 15kHz.

The pressure map of two speakers was measured by creating a diffraction pattern at 12kHz (Fig. 4.10) using two speakers placed at opposite corners of the sensor (as shown in Fig. 4.11.) The two speakers are synchronized in phase, and the current signal at each location is captured by a lock-in amplifier, which is also synchronized with the speakers. The diffraction pattern at

12KHz has a fringe spacing of ≈2.9cm, consistent with the expected fringe distance in air.

The sensitivity (Fig. 4.12) is characterized by comparing with a commercially available microphone, G.R.A.S 40PH microphone. This microphone has a 50mV/Pa sensitivity at 250Hz. By placing our device and the commercial microphone at the same location under an off-the-shelf speaker, we can measure the responses to different levels of sound pressure on the two devices. Our device is characterized to have a sensitivity of 9.5nA/Pa to incoming sound pressure.

The frequency response (Fig. 4.13) is also measured. An off-the-shelf speaker is used here, it has a frequency response ranging from 20Hz to 20KHz. Our device showed a frequency response covering the whole acoustic range. The peaks showing in the frequency response plot is coupling with the frequency response of the speaker.

4.5 Conclusion of the chapter

We have demonstrated a flexible, active matrix microphone using a monolithic architecture that builds an active matrix sensor array on a freestanding piezoelectric polymer. Localized detection of the sound signal is enabled by an active matrix architecture. Our design extends the bandwidth of a locally amplified piezoelectric sheet sensor to the acoustic range, and demonstrates a monolithically integrated active matrix sensing architecture capable of mapping both boundary layer and far field acoustic excitation for a variety of applications.

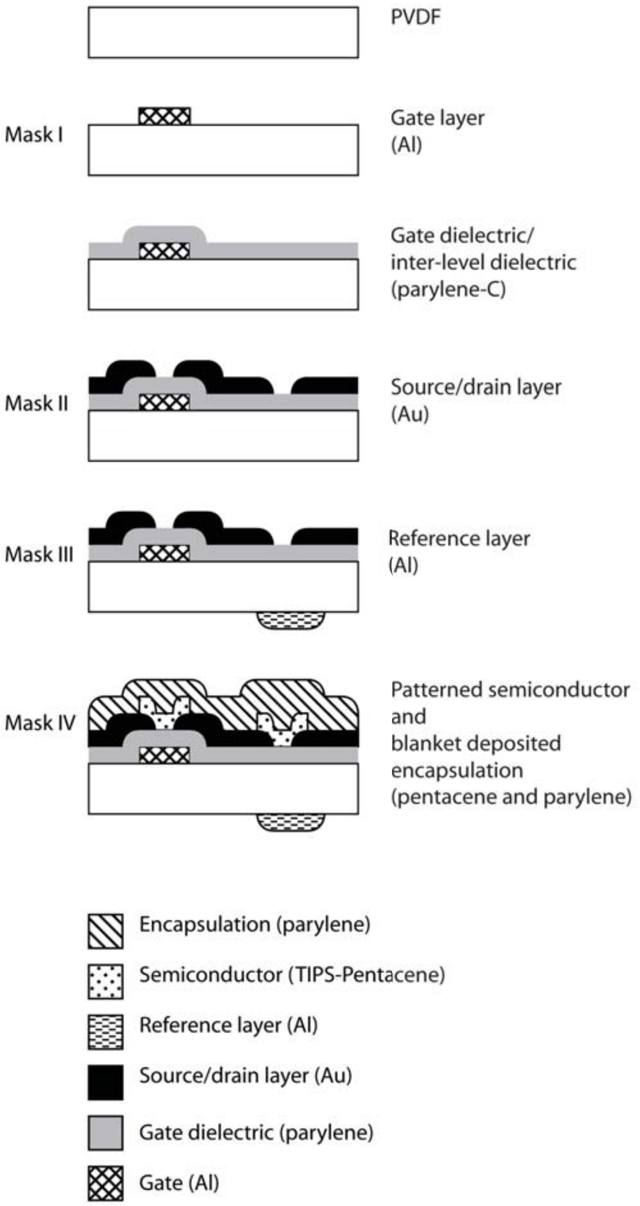

Figure 4.1: Schematic process flow. The pre-poled PVDF (52 microns thick) serves as both the main sensing material and substrate for this device. The switch transistor gate is deposited and patterned, followed by the gate/sensor dielectric, the source/drain and reference electrodes, and the active semiconductor. A layer of parylene-C on top of the final device serves as the passivation at the end.

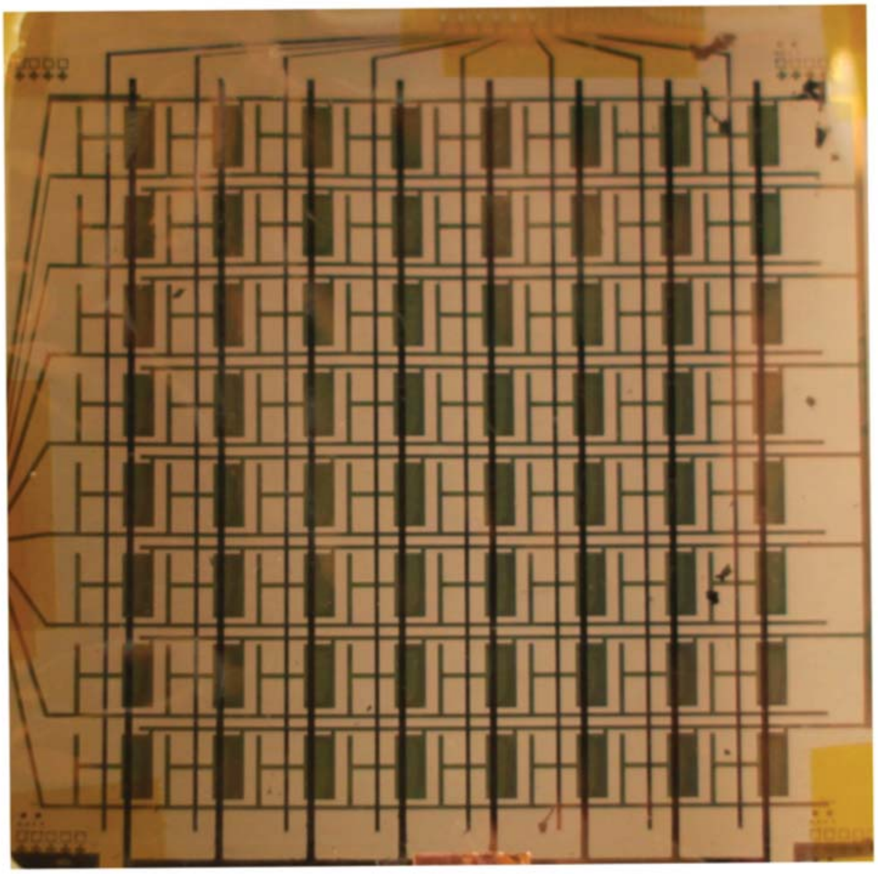

Figure 4.2: The 8X8 active matrix PVDF sensor, X-axis selection is done by switching the gate of the switch transistor on and off with a -20V voltage supply, and Y-axis selection is done by switching the source drain bias (-20V). The switch transistor shares its drain electrode with the source electrode of the sensor transistor.

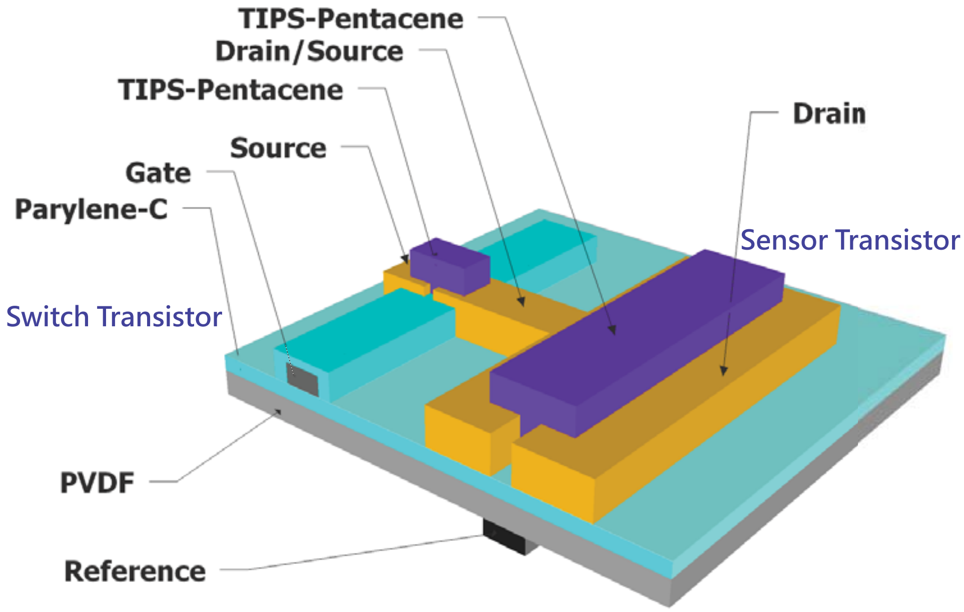

Figure 4.3: The cartoon of a single device. A switch transistor with metal gate is designed to share its drain with the source of the the sensor transistor on its right, which has a larger W/L ratio.

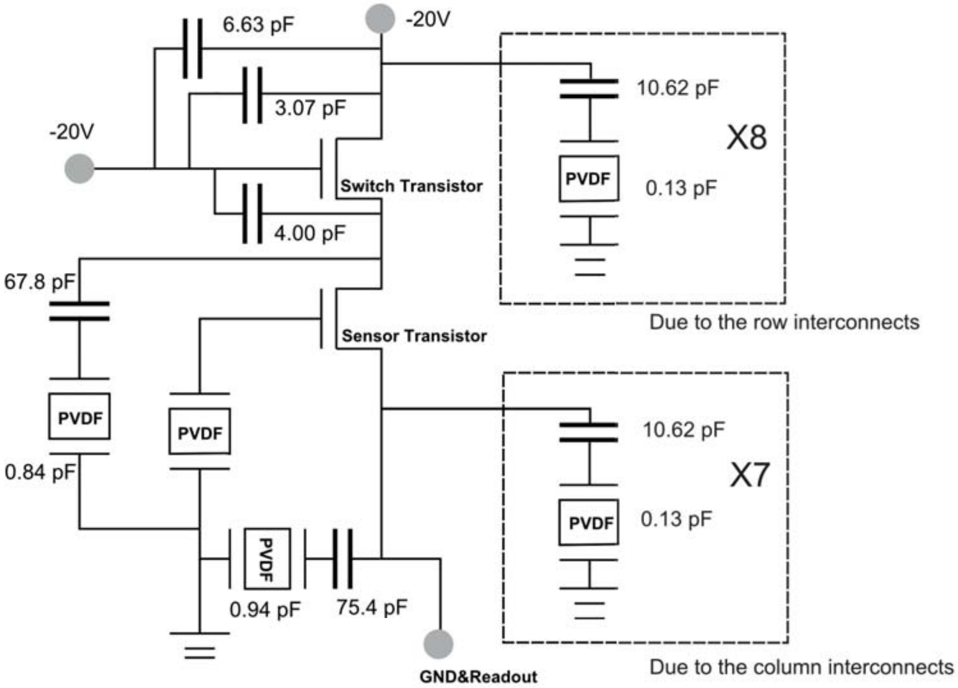

Figure 4.4: The equivalent circuit model of the PVDF microphone. The PVDF film in this model is simulated as a capacitor, and the capacitance is determined by the dimension of the metalized area and the thickness of parylene-c and PVDF. Due to the row and column interconnects, the switch transistor is loaded with a parasitic capacitance as shown in the top right dashed block and the sensor transistor is loaded with a parasitic capacitance as shown in the bottom right dashed block of this diagram.

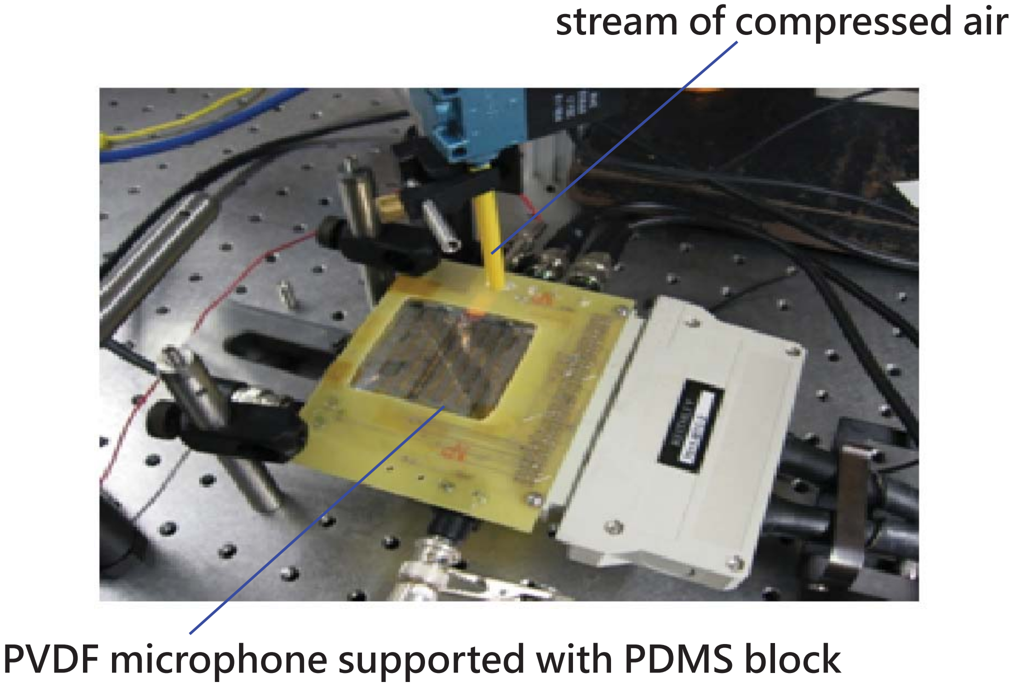

Figure 4.5: The measurement arrangement for Fig. 4.6 and Fig. 4.7. The tube provides the localized air flow used to demonstrate the localization of the piezoelectric response.

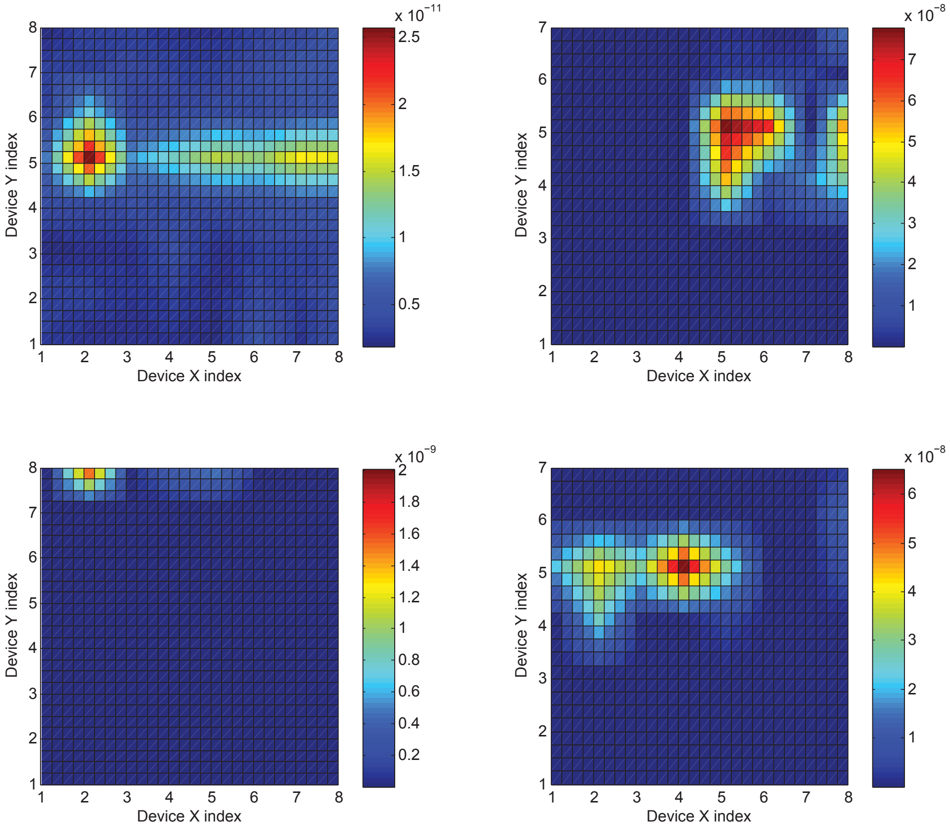

Figure 4.6: A localized map of turbulent air flow from a tube directed to the microphone. This 2D surface map is made with an interpolation factor of 4. The active matrix allows measurement from each of the 64 sites individually. The compressed air current is introduced on four different location on the PVDF microphone sample. Our measurement shows that the PVDF microphone can map the distribution of the compressed air pressure. Edge-induced turbulence from the circuit board can be seen in (5,5), which is the bottom right figure. The microphone can accurately detect the location of the highest level of excitation, which is the spot where the compressed air is applied, as well as the downstream air flow and boundary-related turbulence.

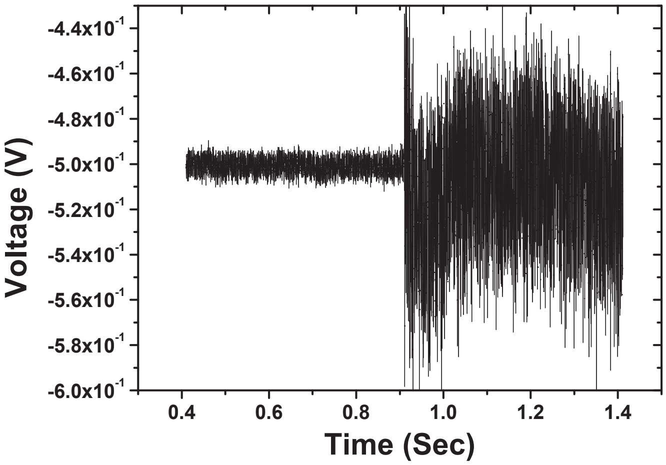

Figure 4.7: The time domain response of a single switched transistor element in response to a stream of compressed gas. The onset of the compressed gas is at 0.9 seconds on the time axis. A large turn-on transient is observed due to the surface deflection, and the interaction of the boundary layer with the piezoelectric generates a charge response which is communicated as a current through the switch and interconnect network. This excitation represents a broadband noise source. The RMS response after the transient is plotted in Fig. 4.6.

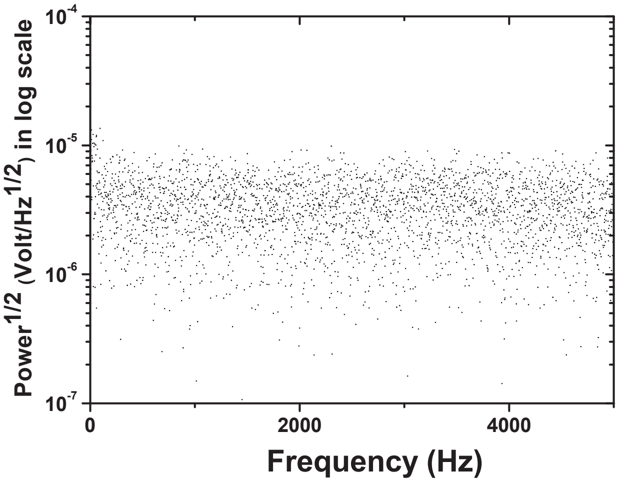

Figure 4.8: The noise floor of the measurement derived from the pre-excitation part of Fig. 4.7. The square root of power versus frequency is plotted here. The noise comes from room acoustic noise, measurement instruments noise, and noise from the switch transistors.

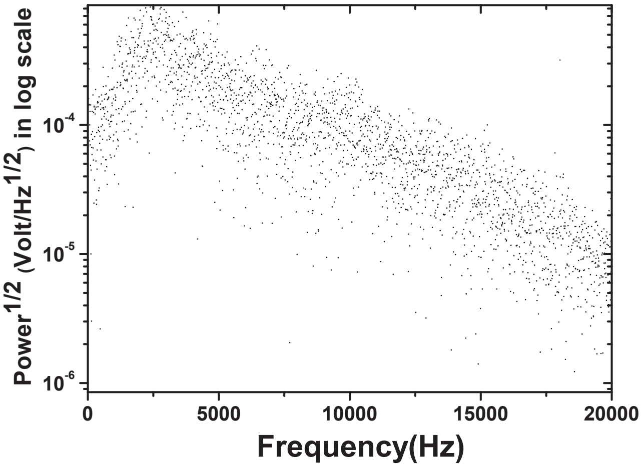

Figure 4.9: Signal frequency composition of the response derived from the post-excitation part of Fig. 4.7. Signal to noise ratio is estimated to be 100 to 1 by comparing this graph with Fig. 4.8, and it reaches 1 when the frequency is around 15kHz, which shows the bandwidth of this device.

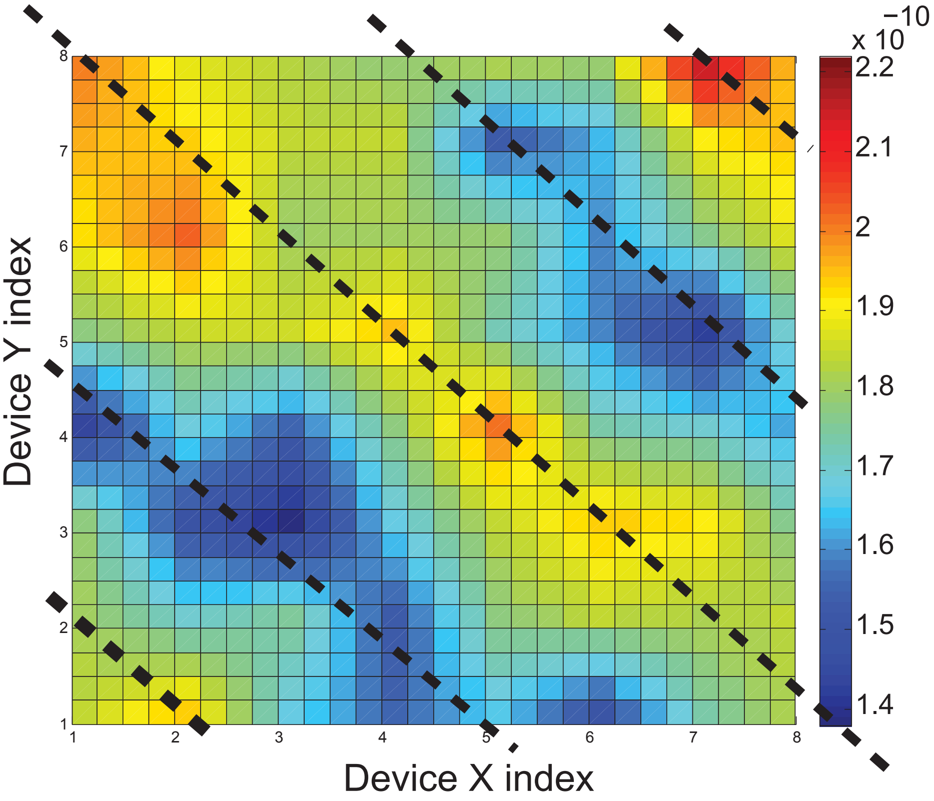

Figure 4.10: An acoustic diffraction pattern at 12kHz (2.9cm) of the amplitude response is plotted here for all 64 sites in interpolated (factor of 4) false color. The dashed lines indicate the interference pattern, which are consistent with the expected fringe spacing.

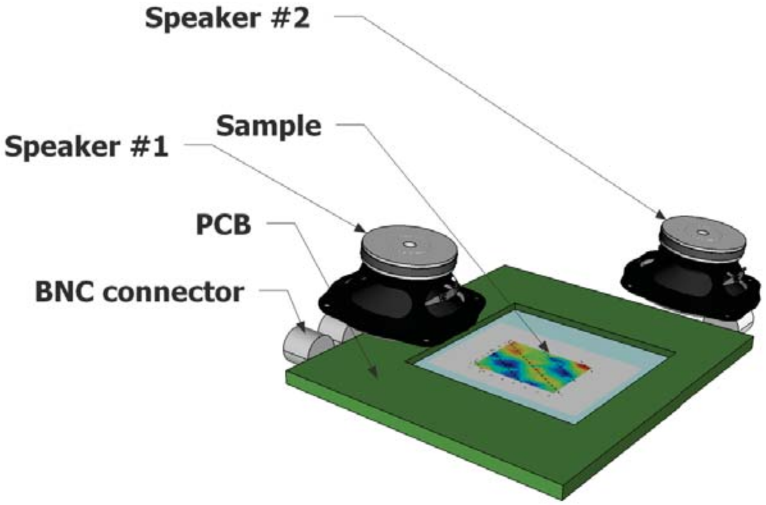

Figure 4.11: The measurement setup for the acoustic diffraction experiment. Two commercially available audio speakers are synchronized in phase and are placed at opposing corners of the microphone to generate the diffraction pattern.

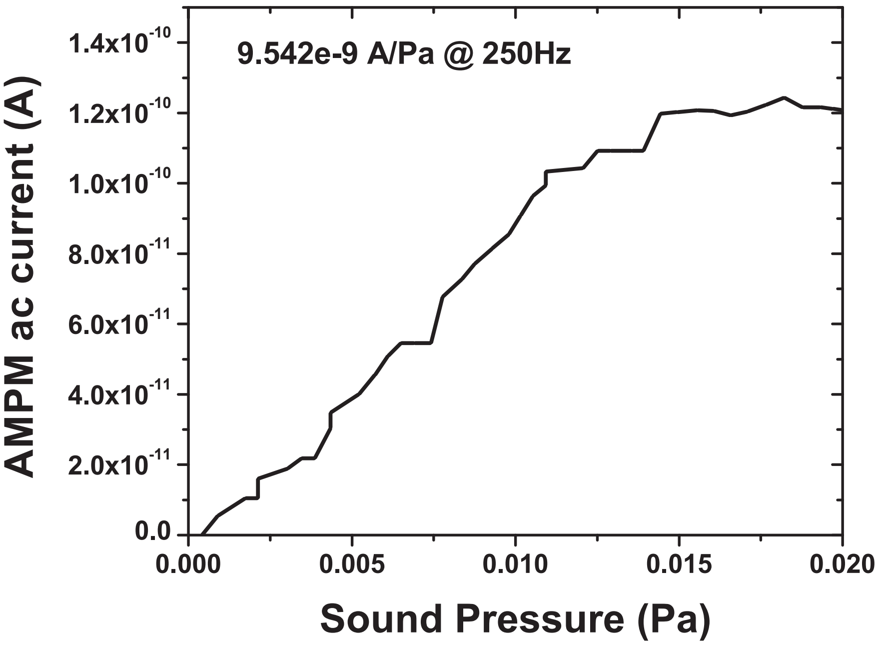

Figure 4.12: The sensitivity curve of the active matrix PVDF microphone element device. Sound pressure is calibrated by using G.R.A.S 40PH microphone. Our device is characterized to have a sensitivity of sound pressure to 9.5nA/Pa.

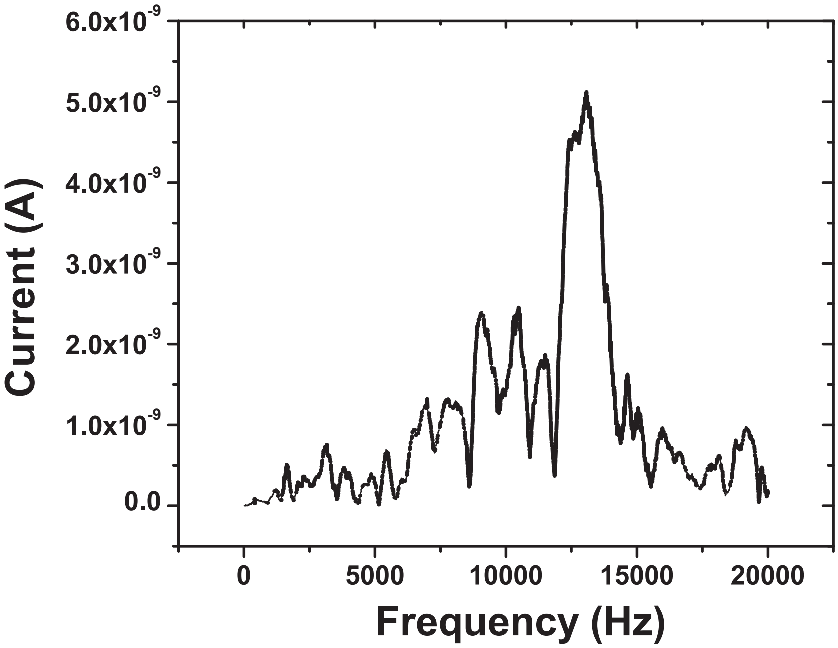

Figure 4.13: Unnormalized frequency response of the active matrix PVDF microphone element device. An off-the-shelf speaker is used here. Our device showed a frequency response covering the whole acoustic range. The peaks showing in the frequency response plot is coupling with the frequency response of the speaker.

Chapter 5

Infrared Pyroelectric Sensor

5.1 Introduction

Heat sensing plays an important role on the world of sensors. Not only living creatures dissipate heat all the time, but also most machines radiate heat when they are at work. Therefore, a variety of applications can be derived from a simple heat sensor.

Household security such as a fire alarm sensor, traffic control such as a vehicle counting device [**?**], and human interface such as a touchless sensor are applications for infrared sensors. In the recent years, research on robots has introduced another application for heat sensors. Using heat sensors to form the E-skin is also a emerging application. Sensing and imaging using IR heat sensors are also found interesting and useful by automobile manufactures. New technologies such as using IR sensor to detect if the driver is dozing and self-driving cars using IR imaging are being developed by many major automobile manufactures.[**?**]

Using pyroelectric material to form IR sensor is one of the most intuitive methods. There are various kind of materials which exhibit pyroelectric property including cesium nitrate ($CsNO_3$), gallium nitride(GaN), lithium tantalate ($LiTaO_3$), and polyvinylidene difluoride (PVDF). Many IR sensors using these materials have been developed.

The pyroelectric property of PVDF was discovered by Bergman et al. in 1971. [?]. Using PVDF with CMOS technology to form arrayed sensor has been demonstrated by Binnie et al. [?] and Munch et al. [?] An integration of organic thin-film transistors with PVDF-trfe on a flexible PET substrate has been shown by Zirkl et al. [?] They have also advanced the design to an active-matrix array for a touchless control interface. [?] [?]

Our goal is to make a infrared sensor that is flexible, equipped with amplifier, easy to fabricate, and low-cost. Therefore, organic thin-film transistors and polyvinylidene difluoride stand out from other materials and become our main elements for making a flexible infrared pyroelectric sensor. A monolithic architecture will be used to fabricate the PVDF IR sensor, thus no glue will be required during the process.

5.2 Pyroelectric response of the PVDF sheet

A simple measurement is conducted to test the pyroelectric response of the PVDF sheet. The electrode deposited on the PVDF sheet has to be thin enough so that it would absorb infrared. Initially, thin aluminum was used for this application, but the transparency and conductivity cannot meet the requirements after multiple attempts. Therefore, sputtered gold(Au)/palladium(Pd) alloy, commonly used as the discharging layer for SEM imaging, is then chosen to replace aluminum as the electrode for PVDF pyroelectric sensor. The overlapped area of the electrodes is $1cm^2$. A time-resolved measurement of the response of a PVDF with Au/Pd electrodes to a desk lamp is shown in Fig. 5.1. The measurement was chopped at 4Hz by an optical chopper placed in front of the PVDF specimen. An incandescent light bulb provides the infrared/heat excitation, and the voltage signal before and after the excitation is recorded by a lock-in amplifier. The result is shown in Fig. 5.1. The signal is increased by 90% after the excitation. Some fluctuations are observed right before the shutter is opened or closed in Fig. 5.1, and they are the piezoelectric response due to the mechanical actuations of the shutter.

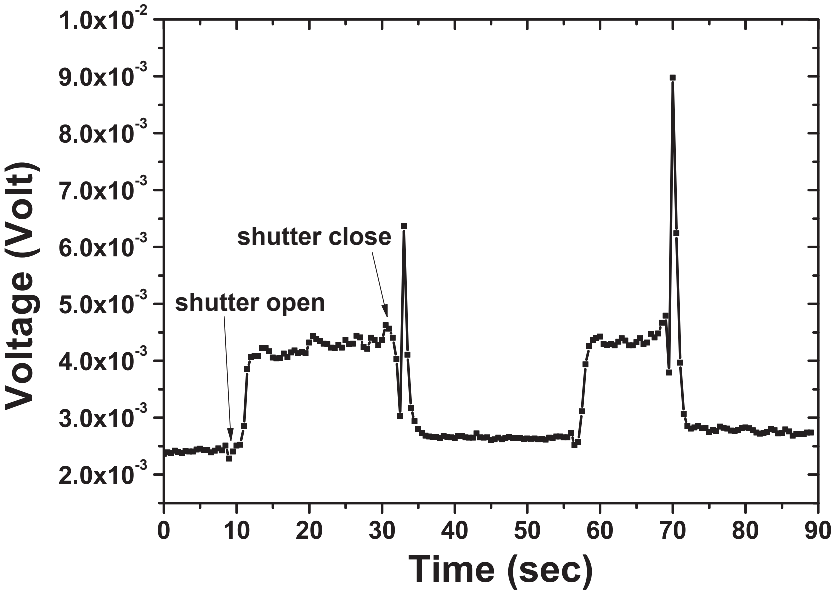

Figure 5.1: Pyroelectric response of a PVDF film coated with 180 $\mathring{A}$ of sputtered Au/Pd electrodes measured with a lock-in amplifier (Standford Research, SR-830). The integration time of the lock-in amplifier is 300 mS, and the sensitivity is set at 50 mV. An incandescent light bulb is used as the IR source and is chopped at 4HZ.

5.3 The integration of OFET and PVDF - Floating gate type

5.3.1 Device design & Fabrication process

A monolithic integration of OFET and PVDF is proposed for this application. By growing organic transistors on one side of the PVDF sheet and depositing a thin layer of Au/Pd on the other side, a device that converts the pyroelectric charge signal to the current signal of the OFET is formed. The schematic diagram of part (b) in Fig. 5.2 shows the device and the designed sensing scheme. The charge generated by the pyroelectric response of PVDF will be mirrored to the interface of parylene-C and pentacene, and it will effectively raise the OFET gate voltage. Therefore the current flowing from source to drain can be modulated by the amount of heat absorbed by the Au/Pd electrode.

The process flow is shown in part (a) of Fig. 5.2. A pre-poled PVDF sheet material provided by Measurement Specialties serves as the substrate and the main sensing material for this application. The PVDF sheet is cleaned with solvents and coated with a layer of parylene-C (230 nm) using CVD. This layer serves as the planarization layer and the dielectric. After the CVD deposition of parylene-C, a thin layer (180 $\mathring{A}$) of Au/Pd is then coated on the other side of the PVDF sheet, and the coating side is chosen to be the positively charged side when pyroelectric effect takes place. This Au/Pd is patterned using a stencil mask to form the reference as well as the IR absorber. After the reference is defined, the sample is flipped for the source/drain electrode deposition. A 40nm-thick gold is deposited with a shadow mask to define the source and drain electrodes. Finally, 250$\mathring{A}$-thick of pentacene is deposited to serve as the active layer of the organic transistor integrated with the PVDF. This is a metal gate-free design similar to the strain sensor structure in chapter. 2, but the reference electrode is replaced with a thin layer of Au/Pd which absorbs IR more efficiently. The finalized sample is shown in Fig. 5.3. UV-Ozone treatment of 20 second is performed in order to increase the transistor current response by shifting the effective threshold voltage.

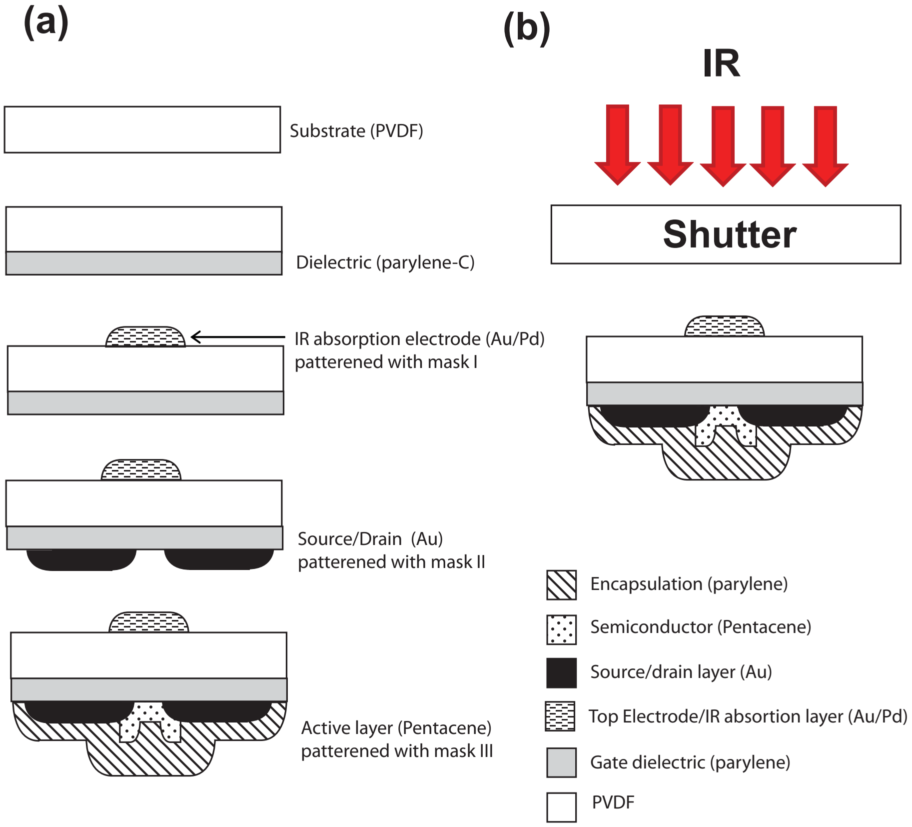

Figure 5.2: Pyroelectric IR sensor. (a) The process flow of an integrated OFET and PVDF sensor element. (b) The schematic diagram of IR excitation to the pyroelectric IR sensor.

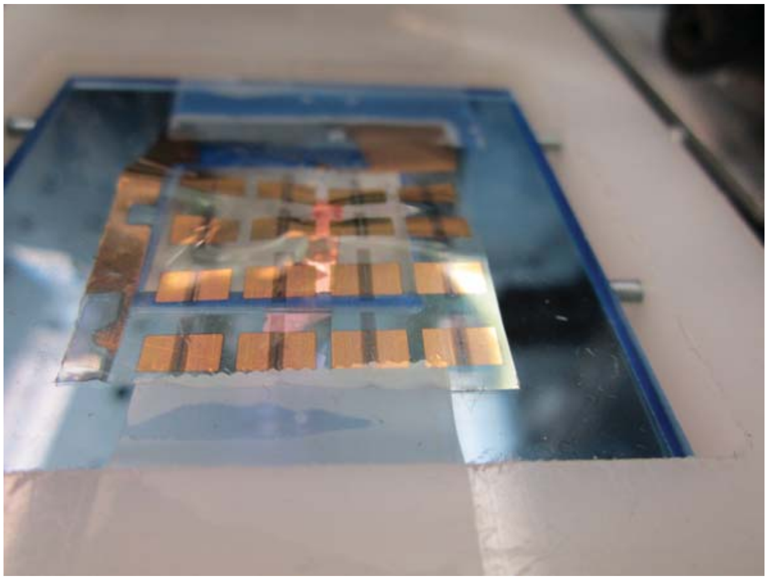

Figure 5.3: PVDF pyroelectric sensor.

5.3.2 Characterization of the floating gate OFET integrated PVDF IR sensor

IR source is a important factor for this measurement, thus the desk lamp used in the previous measurement is replaced with Hawkeye IR-18 infrared source to improve the heat source stability and directionality. This IR emitter is manufactured using a patented silicon nitride material. Their design ensures intrinsic physical and thermal strength. When operated at 12 volts/20 watts the IR-18 reaches 1200°C. This silicon nitride emitter is mounted in a 1 inch parabolic reflector for extremely efficient collimation of energy. Fig. 5.4 shows the IR source and the profile of the heat field emitted by IR-18 when biased at 5V.

Pyroelectric response of the floating gate OFET integrated PVDF IR sensor is shown in Fig. 5.5. When the shutter is opened, the transistor current increases immediately. 15 percent of current increase is observed when the

IR-source is biased at 8V. When the shutter is closed, the current value drops back to its original value. The discharging speed is mainly determined by the heat dissipation rate of the PVDF sheet and the discharging rate through parylene-C layer. Pyroelectric response due to multiple heat stimulations is also conducted, and Fig. 5.6 show the comparison between the OFET current under no stimulation (blue), single shutter open (red), and multiple shutter opens and closes (yellow). It can be seen form figure that the current of different conditions increase at the same rate, but it takes a longer time to decrease back to its neutral value. This could be the thermal effect of the pentacene that is heated at the same time and the trapped charge in the parylene-C layer during the measurement.

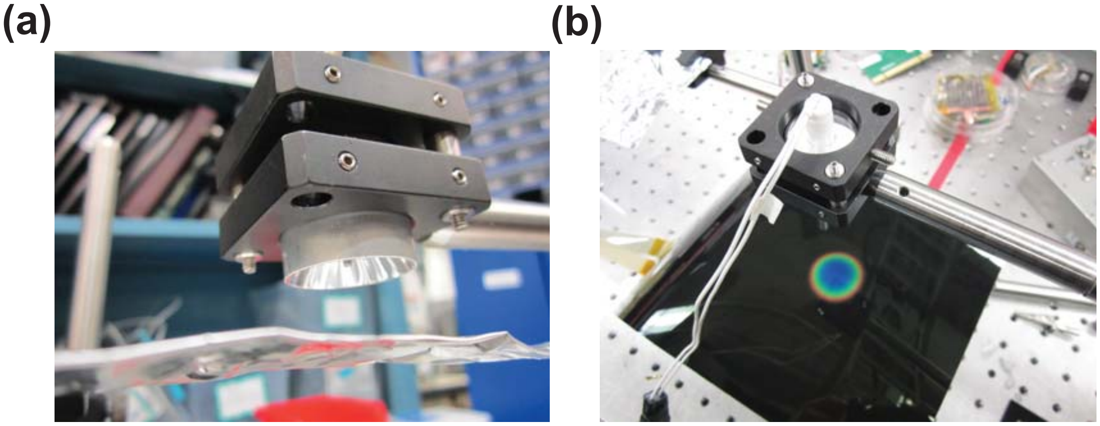

Figure 5.4: (a)The HawkEye IR-18 IR source.(b) The IR profile visualized using temperature sensitive thermochromic sheet (color changing range: 35°C-40°C).

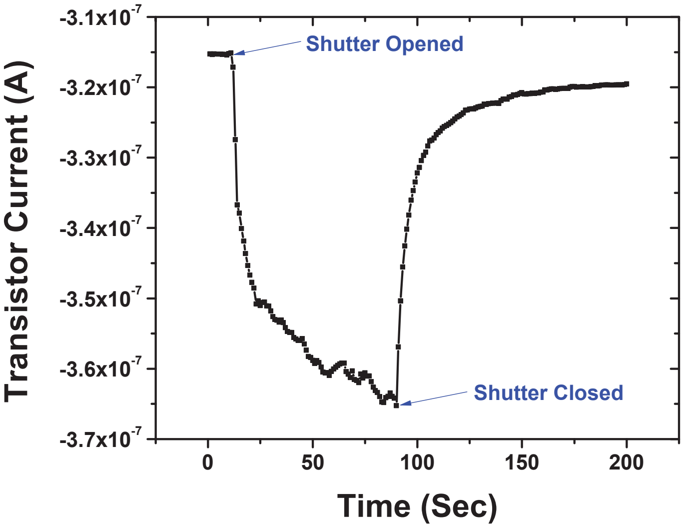

Figure 5.5: Pyroelectric response of the floating gate OFET integrated PVDF IR sensor.

5.4 The integration of OFET and PVDF - Metal gate type

5.4.1 Device design & Fabrication process

The floating gate design in the previous section converts the pyroelectric charge response to the OFET current response. However, the IR shines directly on the transistor channel region, so it could induce the thermal effect and photocurrent of pentacene transistors and further introduce extra factors to the measurement. Therefore, a metal gate OFET integrated PVDF IR sensor is proposed to solve this problem. Fig. 5.7 shows the schematic diagram of this design and the actual sample after fabrication. The fabrication process is similar to the floating gate version of IR sensor, which can be found from Fig. 5.2. However, a metal gate is presented in this design, and the sensing

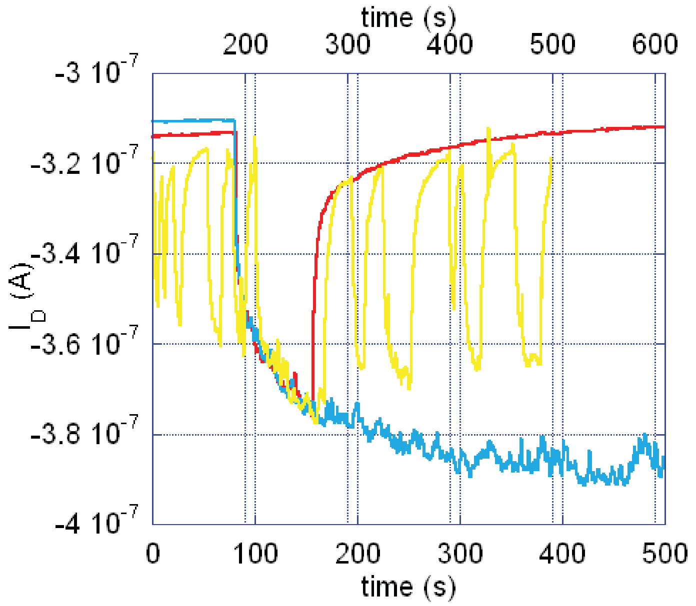

Figure 5.6: The comparison between the current under no stimulation (blue), single shutter open (red), and multiple shutter opens and closes (yellow). Hawkeye IR-18 IR source is used and biased at 8V.

region is now isolated to disambiguate the thermal effect and photocurrent of pentacene. Also, parylene-C layer is patterned using a mask formed by static tape to simplify the structure of the sensing element. The width over length ratio of the transistor is kept at 20 (2000μm/100μm). The pyroelectric response will charge the capacitor formed by PVDF and will provide the gate voltage to modulate the transistor, therefore we can expect a current gain proportional to the increase of IR source temperature. UV-Ozone treatment of 20 second is designed to be used here to shift the threshold voltage of the OFET and make the OFETs work at the linear region.

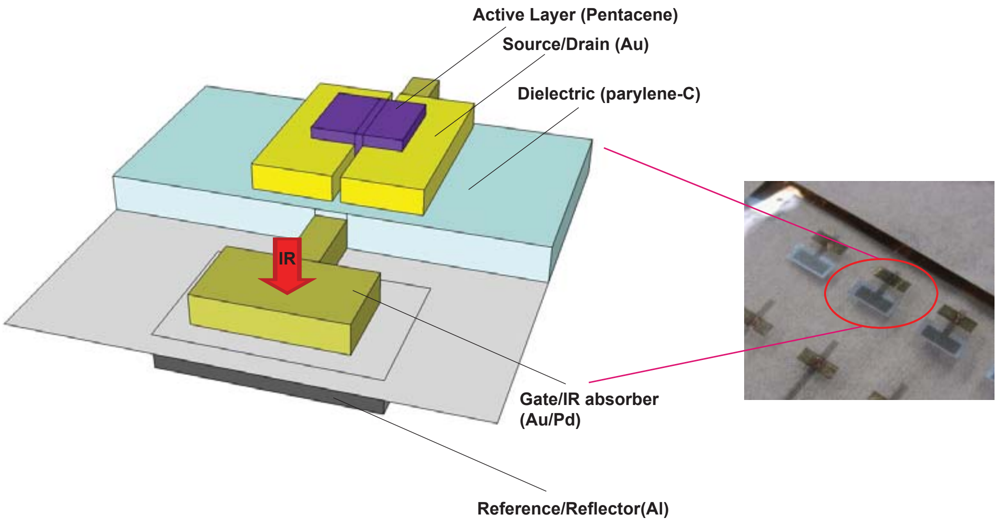

Figure 5.7: The metal gate OFET integrated PVDF IR sensor. The sensing region is isolated and the parylene layer is patterned.

5.4.2 Characterization of the metal gate OFET integrated PVDF IR sensor

The measurement setup is shown in Fig. 5.8. The shutter is controlled by a stepper motor, and the Hawkeye IR-18 IR source provides the IR stimulation. Due to the low Curie temperature (80°C) of PVDF, the surface temperature is monitored and regulated to be always lower than 55°C to ensure the crystal phase of PVDF stays at beta-phase. Keithley 2602 source meter is used to run a time versus OFET current measurement. The time interval is 10 msec, and the total data point is 1000. The shutter opens at least 1 second after the source meter starts recording the OFET current. A short period of stabilization time is observed in the measurements, and this is believed to be the influence of the feedback circuit and auto-ranging circuit in the source meter unit. Since the sensing element is now isolated, the active region of the transistor can be covered to avoid thermal effect and photocurrent.

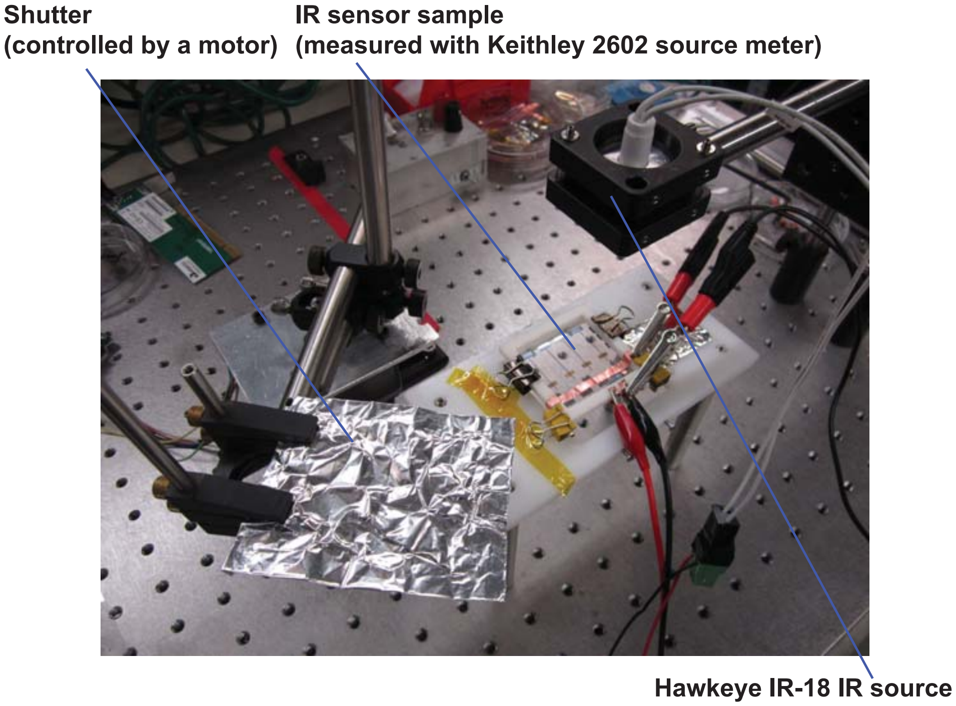

Figure 5.8: The measurement setup of the pyroelectric IR sensor. The aluminum foil shutter is controlled by a stepper motor, and the IR source is regulated to maintain a surface temperature lower than 55°C.

A measurement of the OFET current under no stimulation at room temperature (25°C) is first conducted to find the floor of the signal. The current level is not zero due to the shifted threshold voltage caused by the 20-second UV-Ozone treatment. This measurement is shown as the black curve of Fig. 5.9. After the current value of the neutral position is acquired, the measurements with IR stimulations are conducted to characterize the pyroelectric response of the IR sensor. The IR source is biased at 5V to provide a heat stimulation of ∼46°C. The aluminum foil shutter opens two and half seconds after the measurement begins, and it stays open until the end of the measurement. This measurement is shown as the red curve of Fig. 5.9. A change of 1.95% in current is observed when the IR source is biased to 5V. The shutter is also controlled to open and close for multiple times in order to see the recovery of current. This measurement is shown as the blue curve of Fig. 5.9.

If the charge and discharge rate is determined by the time constant of the capacitor form by PVDF, the parameters form Table.1.1 can be used to estimate the time constant: Given the overlapped area is $5000\mu\text{m} \times 2000\mu\text{m}$ and the thickness of the PVDf film is $52\mu\text{m}$,

$R = \textit{Volume Resistivity} \times \textit{Thickness/Area} = 10^{13} \times 52 \times 10^{-6} / 10^{-5} = 5.2 \times 10^{13}\ (\Omega)$,

$C = \textit{Permitivity} \times \textit{Relative Permitivity} \times \textit{Area/Thickness} = 8.85 \times 10^{-12} \times 12 \times 10^{-5} / 52 \times 10^{-6} = 2.0423 \times 10^{-11} (F)$,

$R \times C = 1062\ (sec)$.

However, this estimated time constant is much longer than what it shows in Fig. 5.9. So we know there is another path through which the charge generated by the PVDF leaks. Fig. 5.10 shows the equivalent circuit diagram of the metal gate OFET integrated PVDF IR sensor. The discharging path is denoted with the red line in the diagram. Since the gate leakage current of 3.35×10^{-11}A is known from the measurement, and the capacitance of the parylene can also be calculated from the overlapped area, the real time constant can be estimated.

$R = \textit{Gate Bias/ Leakage Current} = 10/3.36 \times 10^{-10} = 2.9 \times 10^{10}\ (\Omega)$,

$C = \textit{Permitivity} \times \textit{Relative Permitivity} \times \textit{Area/Thickness of parylene-C} = 8.85 \times 10^{-12} \times 2 \times 10^{-6} / 2300 \times 10^{-10} = 7.69 \times 10^{-11} (F)$,

$R \times C = 2.23\ (sec)$.

This estimated time constant fits the measurement properly, and it also proves our discharge path assumption.

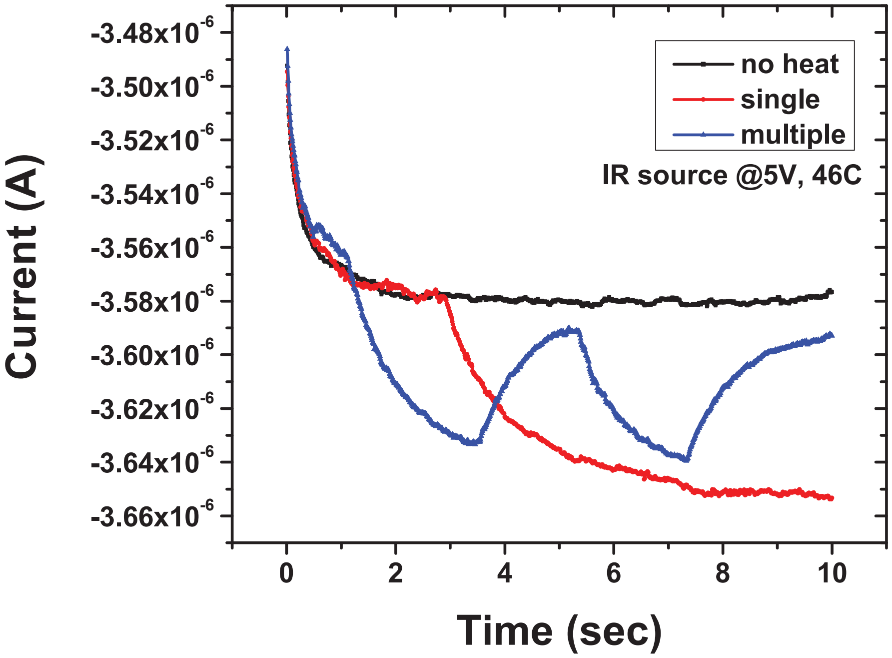

Figure 5.9: Time versus current characteristics at different shutter control conditions. The black curve shows the current response to room temperature, the red curve shows the response of shutter opened once, and the blue curve is the response of shutter opened and closed for two times.

The current response to different temperature stimulation is characterized as well. The IR source is biased at six different level, and the surface temperature of each bias level is measured before the time versus current measurements. Fig. 5.11. shows the results of the current change due to six different temperature stimulations. It can be seen from this graph that the amount of current change is proportional to the temperature difference (room temperature is measured to be 25°C.) The net change of OFET current versus the temperature difference is plotted in Fig. 5.12. These result shows that the pyroelectric response of PVDF is converted to the current response of the integrated OFET, and the OFET current is modulated by

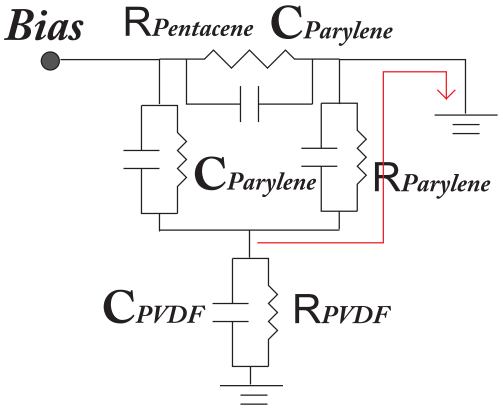

Figure 5.10: The equivalent circuit diagram of the metal gate OFET integrated PVDF IR sensor. The discharging path is denoted with the red line in the diagram.

the charge generated by the PVDF sheet. The responsivity can be estimated to be 3.8nA/°C while the effective sensing area size equals to $1 \times 10^{-4} m^2$.

5.4.3 Flipping the absorber and the reflector

To further improve this design, aluminum is used as the gate as well as the reflector, and Au/Pd is used as the IR absorber (reference electrode) on the other side of the PVDF sheet. The IR stimulation will be applied from the back side (where the absorber is) of the PVDF sheet. Therefore, the aluminum gate will cover the active material (pentacene) completely, reflect the heat, and avoid any thermal effect or photocurrent.

The actual sample of the revised metal gate OFET integrated PVDF IR sensor is shown in Fig. 5.13. It can be seen from the picture that the active region of the transistor is fully covered by its aluminum gate during the measurements, so the thermal effect and photocurrent can be completely avoided.

The pentacene transistors on PVDF substrate is characterized with Keithley 2400 source meter. Fig. 5.14 shows the I_{ds}-V_{ds} characteristics, and Fig. 5.15 shows the I_{ds}-V_{gs} characteristics at V_{ds} = -20V. From these two figures, the threshold voltage can be observed to be positively shifted due to the 20 second UV-Ozone treatment, and the current at $V_{gs} = 0$V is not zero. The transistors are operating in the linear region and stays "on" when there is a source/drain bias.

Hawkeye IR-18 IR source is used to provide the stimulation, and it is raised higher to lower the surface temperature. The measurement setup is identical to the previous measurements of meat gate OFET integrated PVDF IR sensor. The OFET (V_{ds} = -20V) current response to IR stimulation is measured while the reference electrode and the source electrode are grounded. Fig. 5.16 shows the response of the IR sensor when the IR source is biased at 4V (surface temperature = 29°C). The shutter opens at 2.8 second and closes at 6.25 second after the beginning of the measurement. The increase in current is significant in the figure, and the value of change can to be estimated to determine the excitation temperature. However, the change in slope can be used as a better indicator of temperature difference. Fig. 5.16 shows the normalized current response versus ten surface temperatures ranging from 25°C to 34°C. The shutter opens at 2.8 second in this set of measurement. It is clear that the slope decreases dramatically after the shutter is opened. Thus, a calculation of the first-order derivative of the ten curves in Fig. 5.16 at 2.95 second is plotted in Fig. 5.18. A trend of decreasing slope can be observed, and the dependence to temperature is $-7.3\times10^{-5}/$ °C. This relation between the slope and the temperature can be used to estimate the external IR stimulation.

5.5 Conclusion of the chapter

The concept of using OFETs monolithically integrated on freestanding PVDF sheets to form a pyroelectric sensor has been demonstrated. The transistors form a transimpedance amplifier directly at the sensing site, allowing conversion of the pyroelectric charge signal into a current signal which can be externally detected. Gate-free and metal gate architectures are both designed and used, therefore a comparison can be made to disambiguate the thermal effect and photocurrent of pentacene. The response to different level of IR heat is measured to determine the responsisvity to heat temperature. The gate-free design has the largest response to heat, but the response couples with the thermal effect and photocurrent, and the trapped charge in the parylene layer makes it harder to discharge. The metal design uses a PVDF capacitor to provide gate bias to the integrated OFET. The response to heat of metal gate OFET integrated PVDF IR sensor is not as large as the gate-free one, but the thermal effect and the issue of trapped charge is less severe. The last design using Au/Pd absorber and Al gate has the smallest response, but the response to temperature can be characterized using the slope of the current change after the shutter is opened. No thermal effect in the transistors needs to be considered using this design. A flexible, gain-tunable (by changing the source/drain bias), and low-cost IR pyroelectric sensor is proved practical using OFETs and PVDF sheet.

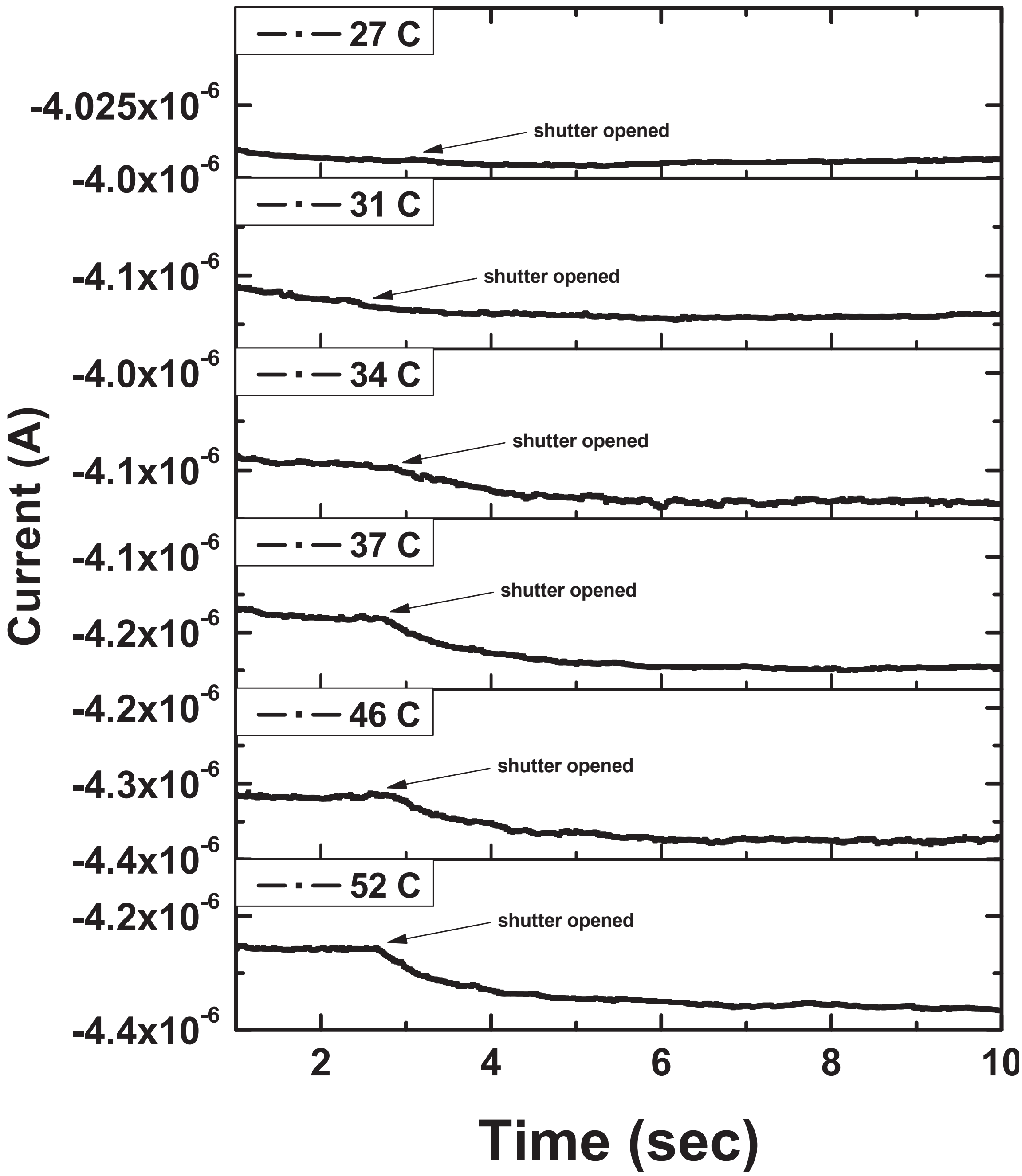

Figure 5.11: Time versus current characteristics at different temperature stimulations

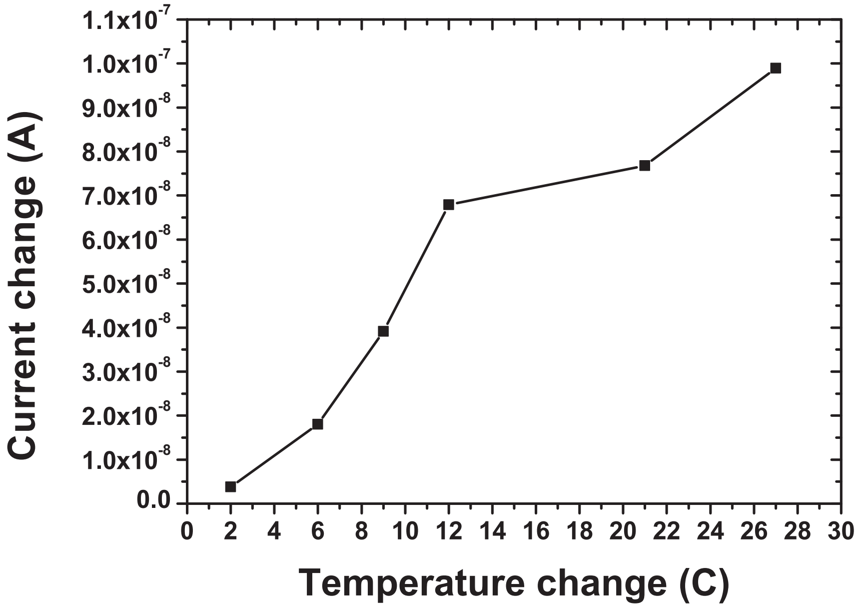

Figure 5.12: Current change versus temperature change. It can be estimated that the responsivity is 3.8nA/°C.

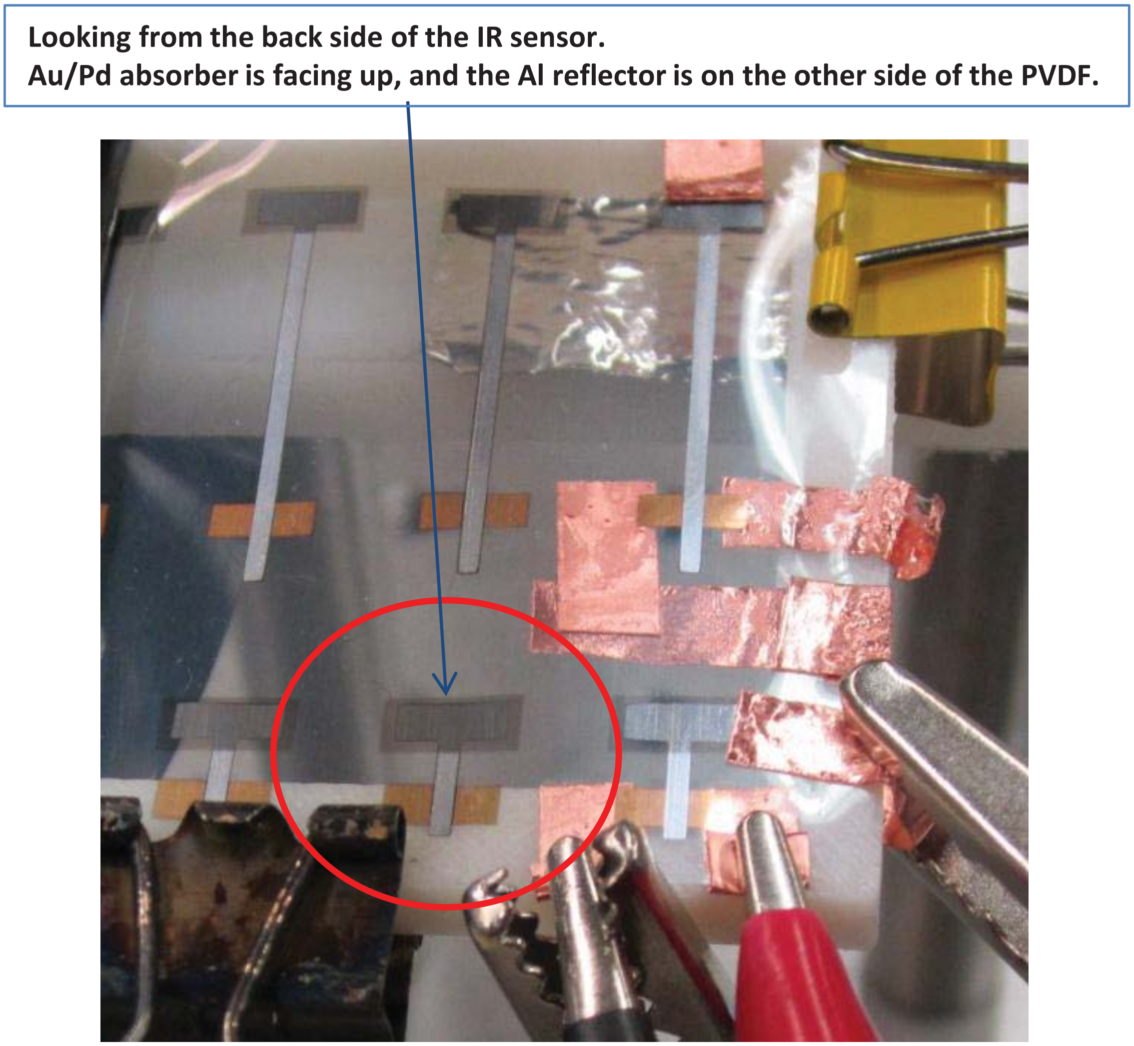

Looking from the back side of the IR sensor.
Au/Pd absorber is facing up, and the Al reflector is on the other side of the PVDF.

Figure 5.13: The IR sensor with Al gate and Au/Pd absorber. The pentacene is fully covered by the aluminum layer, so the IR excitation will be reflected.

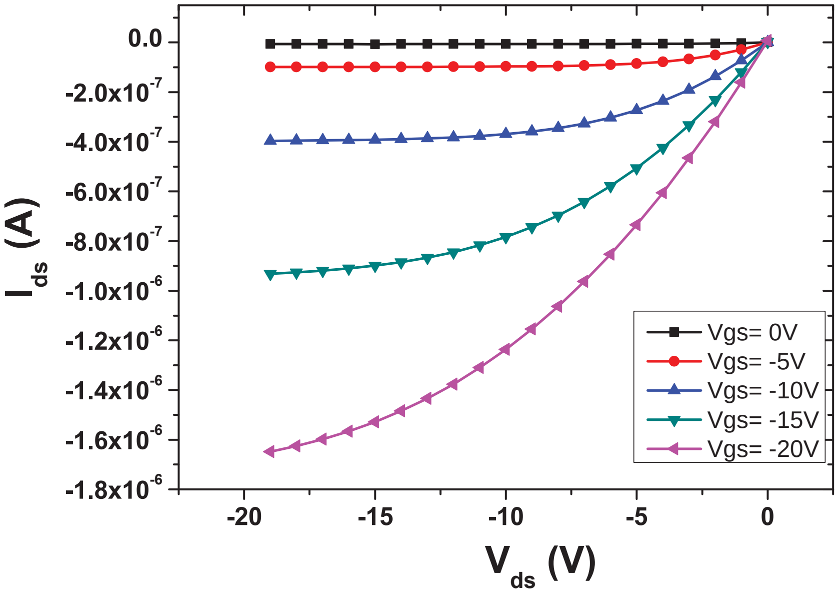

Figure 5.14: The I$_{ds}$-V$_{ds}$ characteristics of the UV-Ozone treated transistor.

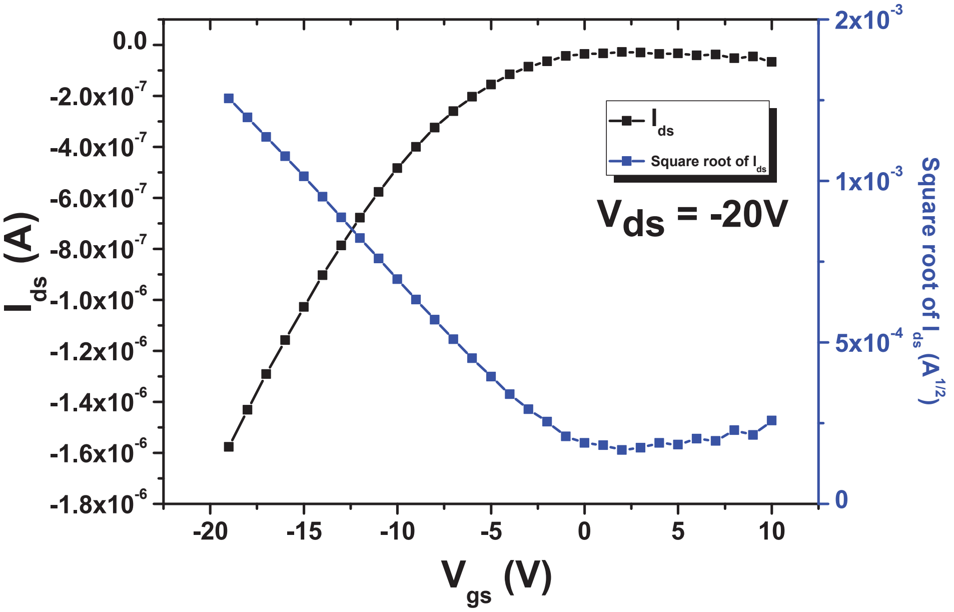

Figure 5.15: The I_{ds}-V_{gs} characteristics of the UV-Ozone treated transistor. V_{ds} is biased to -20V.

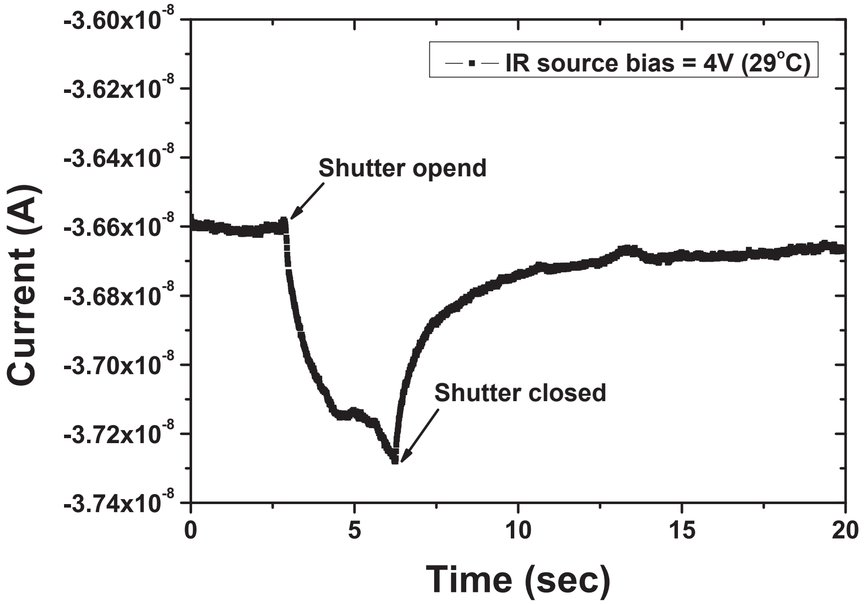

Figure 5.16: The current response of the IR sensor stimulated with a IR source biased at 4V(surface temperature = 29°C).

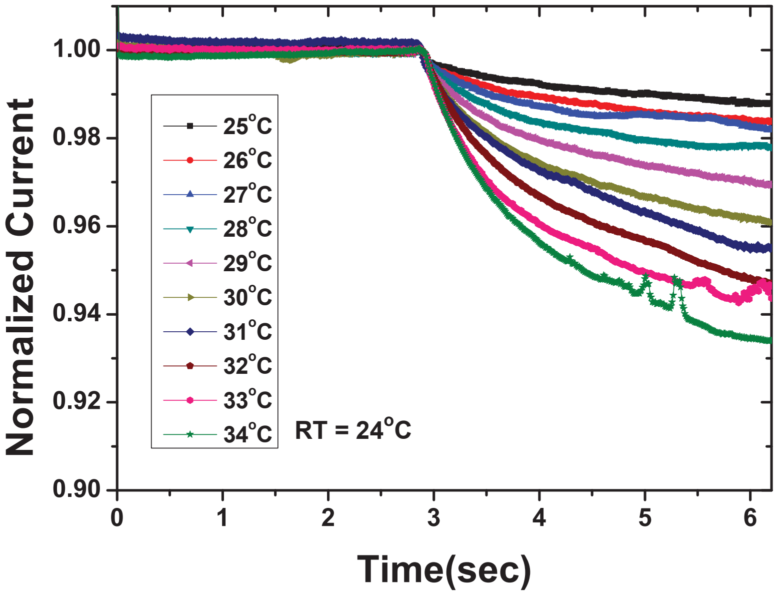

Figure 5.17: The current response to different temperatures, dependence of the IR sensor. The current is normalized to see the change in terms of slope. A shutter made of a sheet of aluminum foil opened at 2.8 second. Room temperature measured by a thermocoupler attached to the PVDF sheet is 24°C.

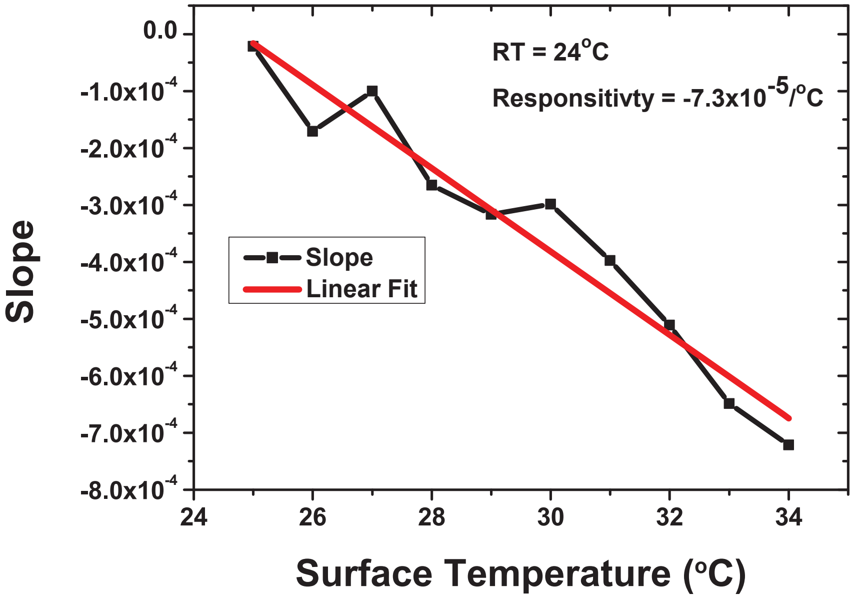

Figure 5.18: The slope (0.15 second after the shutter is opened) of the current response versus surface temperature. A trend of decreased slope is observed as the source temperature increases.

Chapter 6

Conclusion and Future Work

Organic thin film transistors and polyvinylidene difluoride (PVDF) are monolithically integrated to form various kind of sensors. The piezoelectric and pyroelectric property of PVDF provide the sensing capability, and the OFETs converts and amplifies the charge signal from PVDF to a current signal. The problems which previously hindered the research progress of piezoelectric polymer material applications such as parasitics and processing temperature are solved by the integration of OFETs.

The concept of using OFETs monolithically integrated on freestanding PVDF sheets to sense strain or stress has been demonstrated in chapter 2. The transistors form a transimpedance amplifier directly at each sensing site, allowing conversion of the piezoelectric charge signal into a current signal which can be externally detected. The transistors are treated using a process which shifts the threshold voltage positive, allowing measurement of both applied stress and strain. A metal gate-free architecture is also used, which allows for a reasonable charge retention time following actuation.

A tone analyzer was produced in chapter 3 by using a sheet of a piezoelectric polymer material both with and without the transimpedance amplifier (organic thin film transistors). The directly addressed array type, a simple architecture without integrating with organic transistors, proves the concept of producing a distributed resonator with frequency dependent modal response. The integrated organic transistor strain sensor type, a variant of the distributed capacitor array type with transimpedance amplifiers, shows the capability of detecting sound frequency and opens more possibilities for more sophiscated application that can benefit from a amplified current signal. The use of piezoelectric sheet material to determine frequency composition of a single tone by matching the response shape without using any time domain (e.g. FFT) analysis is demonstrated.

Expanded from chapter 2 and chapter 3, a flexible, active matrix microphone using a monolithic architecture that builds an active matrix sensor array on a freestanding piezoelectric polymer is demonstrated in chapter 4. Localized detection of the sound signal is enabled by an active matrix architecture. Our design extends the bandwidth of a locally amplified piezoelectric sheet sensor to the acoustic range, and demonstrates a monolithically integrated active matrix sensing architecture capable of mapping both boundary layer and far field acoustic excitation for a variety of applications.

In chapter 5, the concept of using OFETs and freestanding PVDF sheets to form IR pyroelectric sensor has been demonstrated. Gate-free and metal gate architectures are both designed and characterized. Each design has its advantages and disadvantages. Gate-free design has higher current response to heat but suffered from thermal effect and trapped charge. The metal gate design is less affected by the thermal effect of the transistors, but the change in current is smaller, and the responsivity requires more steps to define and characterize.

A higher resolution for all the sensors in this work will make it even easier to use these sensors to the real world applications. Besides, a faster switching speed of the integrated transistors can also be achieved by using a more advanced fabrication process. In the future, the strain sensor in chapter 2 can be integrated with an active matrix to improve its resolution and increase the sensing speed, the tone analyzers in chapter 3 can have improved sound frequency resolution with more devices on the PVDF sheet, the active matrix microphone in chapter 4 needs a denser array and a higher current response from the sensing site to improve its spatial resolution and detectivity, and a matrixed version of the IR pyroelectric sensors could make it open to more applications.